JGR Solid Earth

RESEARCH ARTICLE
10.1029/2022JB024683

On the Choice and Implications of Rheologies That Maintain Kinematic and Dynamic Consistency Over the Entire Earthquake Cycle

Rishav Mallick[1,2], **Valère Lambert**[3], **and Brendan Meade**[4]

[1]Seismological Laboratory, California Institute of Technology, Pasadena, CA, USA, [2]Earth Observatory of Singapore, Nanyang Technological University, Singapore, Singapore, [3]Seismological Laboratory, University of California, Santa Cruz, NC, USA, [4]Department of Earth and Planetary Sciences, Harvard University, Cambridge, MA, USA

Abstract Viscoelastic processes in the upper mantle redistribute seismically generated stresses and modulate crustal deformation throughout the earthquake cycle. Geodetic observations of these motions at the surface of the crust-mantle system offer the possibility of constraining the rheology of the upper mantle. Parsimonious representations of viscoelastically modulated deformation through the aseismic phase of the earthquake cycle should simultaneously explain geodetic observations of (a) rapid postseismic deformation, (b) late in the earthquake cycle near-fault strain localization. To understand how rheological formulations affect kinematics, we compare predictions from time-dependent forward models of deformation over the entire earthquake cycle for an idealized vertical strike-slip fault in a homogeneous elastic crust underlain by a homogeneous viscoelastic upper-mantle. We explore three different rheologies as inferred from laboratory experiments: (a) linear Maxwell, (b) linear Burgers, (c) power-law. The linear Burgers and power-law rheologies are consistent with fast and slow deformation phenomenology over the entire earthquake cycle, while the single-layer linear Maxwell model is not. The kinematic similarity of linear Burgers and power-law models suggests that geodetic observations alone may be insufficient to distinguish between them, but indicate that one may serve as an effective proxy for the other. However, the power-law rheology model displays a postseismic response that is non-linearly dependent on earthquake magnitude, which may offer a partial explanation for observations of limited postseismic deformation near some magnitude 6.5–7.0 earthquakes. We discuss the role of mechanical coupling between frictional slip and viscous creep in controlling the time-dependence of regional stress transfer following large earthquakes and how this may affect the seismic hazard and risk to communities living close to fault networks.

Plain Language Summary The solid Earth is a viscoelastic material that displays both solid and fluid-like behaviors depending on the observational time window and the applied stress. We develop numerical simulations of how the uppermost solid Earth responds to a sequence of periodic earthquakes and the earthquake cycle. Our simulations test a range of proposed viscoelastic materials. The predicted surface displacements from each model are compared with observational features extracted from geodetic datasets compiled over the past few decades. All existing viscoelastic material descriptions can satisfactorily explain observational features in the first few years following an earthquake; significant differences between the viscoelastic models emerge 10–100 years following a large earthquake. Identifying the most appropriate viscoelastic description requires the integration of geodetic data that constrains the velocity evolution from a sequence of earthquakes (as opposed to a single event) with observations from rock physics laboratory experiments. A unified description of visceolasticity in the uppermost solid earth has important implications for understanding stress evolution in fault networks, and improving models of seismic hazard.

Key Points:

- We develop a kinematically consistent periodic earthquake cycle model with mechanical coupling between frictional slip and viscous creep
- Steady-state power-law and linear Burgers rheologies are consistent with earthquake cycle observations while linear Maxwell is not
- Distributed viscous creep alters the (stress) loading rate of a large volume around the fault and is important for multifault interactions

Correspondence to:
R. Mallick,
rmallick@caltech.edu

Citation:
Mallick, R., Lambert, V., & Meade, B. (2022). On the choice and implications of rheologies that maintain kinematic and dynamic consistency over the entire earthquake cycle. *Journal of Geophysical Research: Solid Earth*, *127*, e2022JB024683. https://doi.org/10.1029/2022JB024683

Received 28 APR 2022
Accepted 14 SEP 2022

Author Contributions:
Conceptualization: Rishav Mallick, Valère Lambert, Brendan Meade
Methodology: Rishav Mallick, Valère Lambert
Software: Rishav Mallick, Valère Lambert
Validation: Rishav Mallick, Brendan Meade
Writing – original draft: Rishav Mallick, Valère Lambert, Brendan Meade
Writing – review & editing: Rishav Mallick, Valère Lambert, Brendan Meade

1. Introduction

Inferring the constitutive relations that describe how the macroscopic stress state of the lithosphere-asthenosphere system evolves as a function of strain rate, total strain, and intensive system variables (temperature, pressure, composition, etc.) remains a grand challenge in the geosciences (NSF, 2020). Constraining these constitutive relations, or rheology, is fundamental to our understanding of the dynamics of the solid Earth. From the occurrence of earthquakes and their effects at any point within the Earth, to the construction of the geological structure that surrounds us and the sustenance of plate tectonics itself, the rheology and strength of Earth materials

plays a crucial role in defining these processes (Bürgmann and Dresen, 2008; Mulyukova and Bercovici, 2019). However, inferring these constitutive relations at the kilometer scale of geological processes is a difficult task as aspects of rock failure are shown to be scale-dependent (e.g., Lambert et al., 2021; Yamashita et al., 2015) and there are limited opportunities to conduct experiments at the crustal or lithospheric scale. Our goal in this article is to demonstrate that the earthquake cycle, in the vicinity of a mature strike-slip fault, may provide us with the necessary experimental conditions to probe the rheology of the lithosphere.

While there exist a number of studies that have sought to infer rheological properties of Earth's lithosphere-asthenosphere system using observations from the earthquake cycle (Bürgmann and Dresen, 2008, and references therein), the interpretation of results from different methodologies for extracting rheological parameters can be limited or challenged by three key assumptions. First, a common approach to modeling geophysical systems is to prescribe a functional form of the rheological model a priori and then estimate the associated best-fitting set of rheological parameters for that selected model, potentially with limited consideration of alternative rheological models that may be equally or better supported by the observations. Second, studies are often limited to a specific observational time window, such as a few years following an earthquake, from which the aforementioned best-fit model parameters are estimated. As such, inferred parameters are tied to the observational window that is probed, which may in part explain vastly different rheological estimates determined for studies of the lithosphere over different observational windows (e.g., Henriquet et al., 2019; Hussain et al., 2018; Kaufmann & Amelung, 2000; Larsen et al., 2005; Milne et al., 2001; Pollitz, 2005, 2019; Ryder et al., 2007; Tamisiea et al., 2007). Finally, a common assumption when processing observed time series is that the signal can be well-separated into a set of linearly superimposed functions, thereby neglecting nonlinear interactions among the associated physical processes.

In this work, we seek to develop a framework that overcomes some of these limitations and can reconcile rheological inferences from different observational windows. As a starting point, we focus on major observational features in geodetic time series obtained from mature strike-slip fault settings globally, from immediately following earthquakes (postseismic period) to late in the earthquake cycle (interseismic period). We do not attempt to directly optimize the fit to data, rather we consider the generality and descriptive power of popular rheological models of the lithosphere and study where each model can explain major observational features or is insufficient (Tarantola, 2006). To assist the reader with appreciating the task at hand, we begin by providing some background on common rheological models that are used to describe lithospheric deformation, general observational constraints available from geodesy and prevalent modeling strategies in the literature.

1.1. Elasticity, Friction and Viscous Creep

The rheology of the lithosphere does not appear to follow a single simple description at all timescales. For example, observations of the passage of seismic waves and the static deformation of the Earth's lithosphere, in response to an earthquake, allow us to describe the lithosphere as an elastic body over timescales ranging from seconds to a day. However, the entire lithosphere cannot be elastic since an earthquake source is a frictional rupture restricted to a narrow shear band (Kanamori & Brodsky, 2004). At timescales longer than a day, time-dependent deformation patterns of the solid Earth's surface following large earthquakes reveal the nonelastic nature of the lithosphere, that is, deformation that continues well after the initial source of deformation has ceased, and is thought to result from a combination of two different processes: (a) time-dependent frictional slip on fault planes (afterslip) while the surrounding medium is elastic (Marone et al., 1991), and (b) time-dependent distributed deformation of the entire medium itself. This is commonly modeled as a viscoelastic process where the short timescale stress perturbations are accommodated by the elasticity of the medium ($\varepsilon \propto \sigma$), while relaxation following instantaneous stress steps or long timescale observations highlight the viscous properties of the medium, that is, $\dot{\varepsilon} \propto \sigma^n$ (ε—strain, $\dot{\varepsilon}$—strain rate, n—power exponent, σ—stress) (Hirth & Kohlstedt, 2003). Laboratory experiments also suggest that viscous flow laws exhibit unsteady or transient deformation, that is, the relationship between σ and $\dot{\varepsilon}$ is unique once steady state is achieved, which requires a finite amount of strain or time (Post, 1977). This style of deformation is often modeled using a Burgers rheology (e.g., Hetland & Hager, 2005; Müller, 1986).

1.2. Geodetic Observations

In this study, we focus on mature strike-slip faults and simplify them to a two-dimensional geometry and describe the characteristics of the interseismic and postseismic period as imaged by the past few decades of geodetic

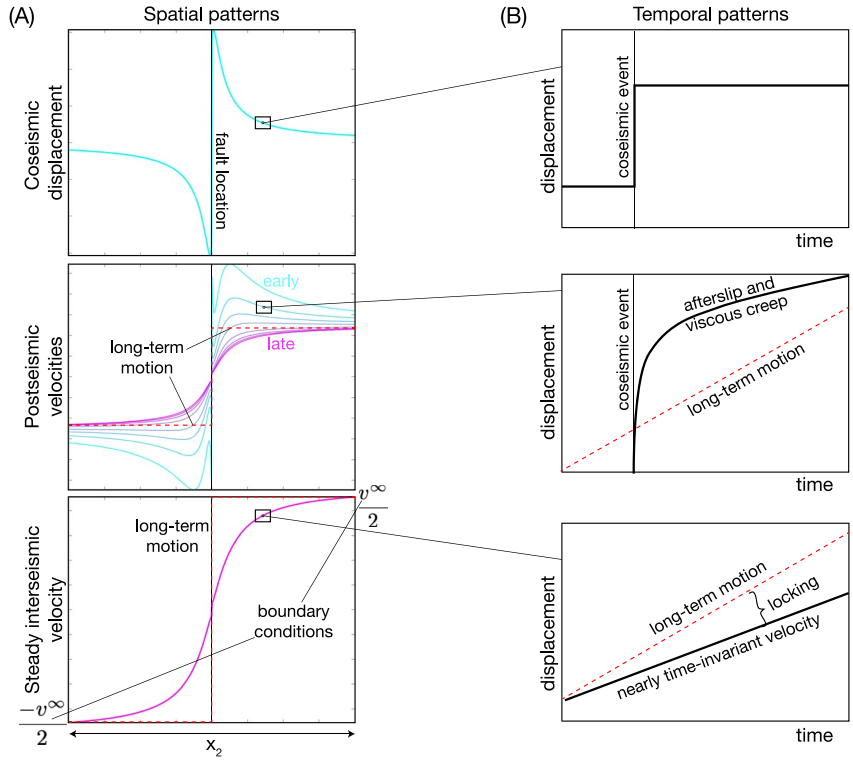

Figure 1. Schematic displacement and velocity evolution recorded at the Earth's surface over the entire earthquake cycle. We show both (a) the spatial pattern (in colors varying from blue—early postseismic, to pink—late postseismic) and (b) the temporal evolution at a chosen location (black lines). The geodetic predictions from steady rigid block motion is shown in red-dashed lines, and deviations from this motion arise due to effects of the earthquake cycle.

observational techniques; these are (a) the interseismic locking depth, (b) the postseismic relaxation time, and (c) cumulative postseismic deformation over a given time window. These are key features that numerical models of earthquake cycles along such faults attempt to explain.

1.2.1. Interseismic Observations

In between earthquakes, geodetic time series from most mature strike-slip fault settings appear nearly linear in time, at least over available observational timescales (1–2 decades), and the estimated velocities follow an S-shaped function in space (Figure 1), commonly modeled using the functional form $\frac{v^\infty}{\pi}\tan^{-1}\left(\frac{x}{D_{lock}}\right)$ (Savage & Burford, 1973) where v^∞ is the estimated long-term slip rate on the fault and D_{lock} is the depth to which the fault is locked. The estimated locking depth from this kind of modeling is on the order of 10–20 km, which is comparable to the thickness of the lithosphere over which frictional processes are thought to be dominant (Vernant, 2015). Deviations from this expected behavior do appear in the data, such as nonlinearities in the time series and deviations from the $\tan^{-1}$ shape function, however, these differences are mostly due to localized creep episodes (in time and space) or time-invariant creep on some sections of the fault (e.g., Khoshmanesh & Shirzaei, 2018; Mallick et al., 2021; Burgmann, 2018).

1.2.2. Postseismic Observations

Following large earthquakes, time-dependent deformation occurs in the near-field as well as far away from the fault. This time-dependent signal is typically decomposed into a linear term and a decaying curvature term (Figure 1). The linear term is assumed to represent background loading due to the motion of tectonic plates, as discussed above. The curvature in the time series is typically fit with functional forms such as $\sim\log(t)$ and $\sim e^{-t}$, motivated by spring-slider models of afterslip and creep of a linear viscoelastic material, respectively (Perfettini & Avouac, 2004). Poroelastic deformation can also contribute to postseismic deformation (Jónsson et al., 2003; Peltzer et al., 1998), however, we ignore this process as we are limited to a two-dimensional anti-plane geometry where no volumetric strains occur.

1.3. The Underlying Physical and Computational Problem

The goal is to infer the rheology of the fault and surrounding medium from the spatio-temporal pattern of surface deformation that contain the features described in the previous section. Two predominant modeling strategies are used for such studies—kinematic modeling of the deformation field and parameter estimation using dynamic models.

1.3.1. Kinematic Models

Kinematic models use principles of linear elasticity to develop an impulse-response type relationship between unit inelastic shear and displacements at the Earth's surface (e.g., Barbot, 2018; Segall, 2010). This set of linear relationships is then used to construct a set of normal equations to estimate slip or strain distributions within the discretized domain to explain the data. The results of such an exercise are estimates of the inelastic source deformation (fault slip—$\Delta s(t)$ and distributed strain—$\Delta\varepsilon(t)$), which then may be combined with elastic stress computations to estimate the relationship between stress change and incremental slip/strain and other derived quantities.

1.3.2. Dynamic Models

Dynamic models typically perform physics-based simulations to solve for the stress (σ) and strain-rate evolution ($\dot{\varepsilon}$) within the Earth's lithosphere consistent with quasistatic equilibrium: $\nabla \cdot \sigma(\dot{\varepsilon}) + \mathrm{f}_b = 0$. f_b is the equivalent body force applied to the system, which could arise from gravity or imposed slip and tractions as a boundary condition (e.g., Segall, 2010). To obtain a unique solution for each simulation, boundary conditions and initial conditions need to be specified. Most simulations apply mixed boundary conditions along the edge of the domain (e.g., Figure 2a). However, the choice of initial conditions remains a difficult task. Many studies treat the pre-earthquake strain rate as a free parameter that is also estimated as part of the inverse problem. The end goal is to determine the coefficients relating σ and $\dot{\varepsilon}$; to do that, an optimization is performed such that the misfit between predicted deformation and the observed deformation time series at sites on the Earth's surface is minimized.

1.3.3. Decomposing the Time Series

To simplify the inverse problem, many kinematic and dynamic modeling studies decompose the observed tectonic deformation time series into additive contributions arising from (a) a constant in time but spatially variable velocity field and (b) residual terms that are supposed to correspond to time-dependent postseismic deformation (Figure 1). This simplification helps split the spatial domain of the problem into a computationally convenient framework—by neglecting the spatially variable velocity field, post-earthquake relaxation studies need only model inelastic deformation sources that satisfy a zero-displacement boundary condition; a condition that is satisfied trivially for a finite deformation source. A point to note is that this linear decomposition of the time series holds exactly for linear dynamical systems, but can be a source of error and bias if the rheology is nonlinear.

1.3.4. Viscoelastic Earthquake Cycle Models

To circumvent issues related to far-field boundary and initial conditions, as well as data decomposition, numerical studies can focus on periodic earthquake cycles. These class of models have been developed in an effort to predict and explain time-dependent earthquake cycle deformation consistent with not only a single earthquake, but also the cumulative effects of periodic earthquake sequences integrated over time (across 10's or 100's of earthquakes) to reach an approximately cycle invariant state.

Analytic and semi-analytic interseismic velocity models have been developed assuming linear viscoelastic rheologies in both the cases of a finite thickness faulted elastic layer over an unbounded viscoelastic region (Cohen & Kramer, 1984; Hetland & Hager, 2005, 2006; Savage & Prescott, 1978), depth-averaged rheology models (Lehner & Li, 1982; Li & Rice, 1987; Spence & Turcotte, 1979), as well as a thin viscoelastic channel (Cohen & Kramer, 1984). These models use linear Maxwell or Burger's rheologies (Hetland & Hager, 2005) to describe the viscoelastic medium and assume that earthquakes rupture the entire elastic layer. More recent studies account for the mechanical coupling between afterslip and viscoelastic deformation. Since these models involve linear rheologies, the effect of velocity boundary conditions is weak, and the inverse exercise simply involves fitting the curvature in the data with an optimum value of the viscosity (or viscosities for a Burger's body) of the system.

An alternative approach is to incorporate rheological parameterizations based on laboratory experiments when solving for equilibrium conditions. These laboratory-derived rheological models are typically determined from studies of single crystal or polycrystal assemblages of minerals thought to be the dominant deforming phase

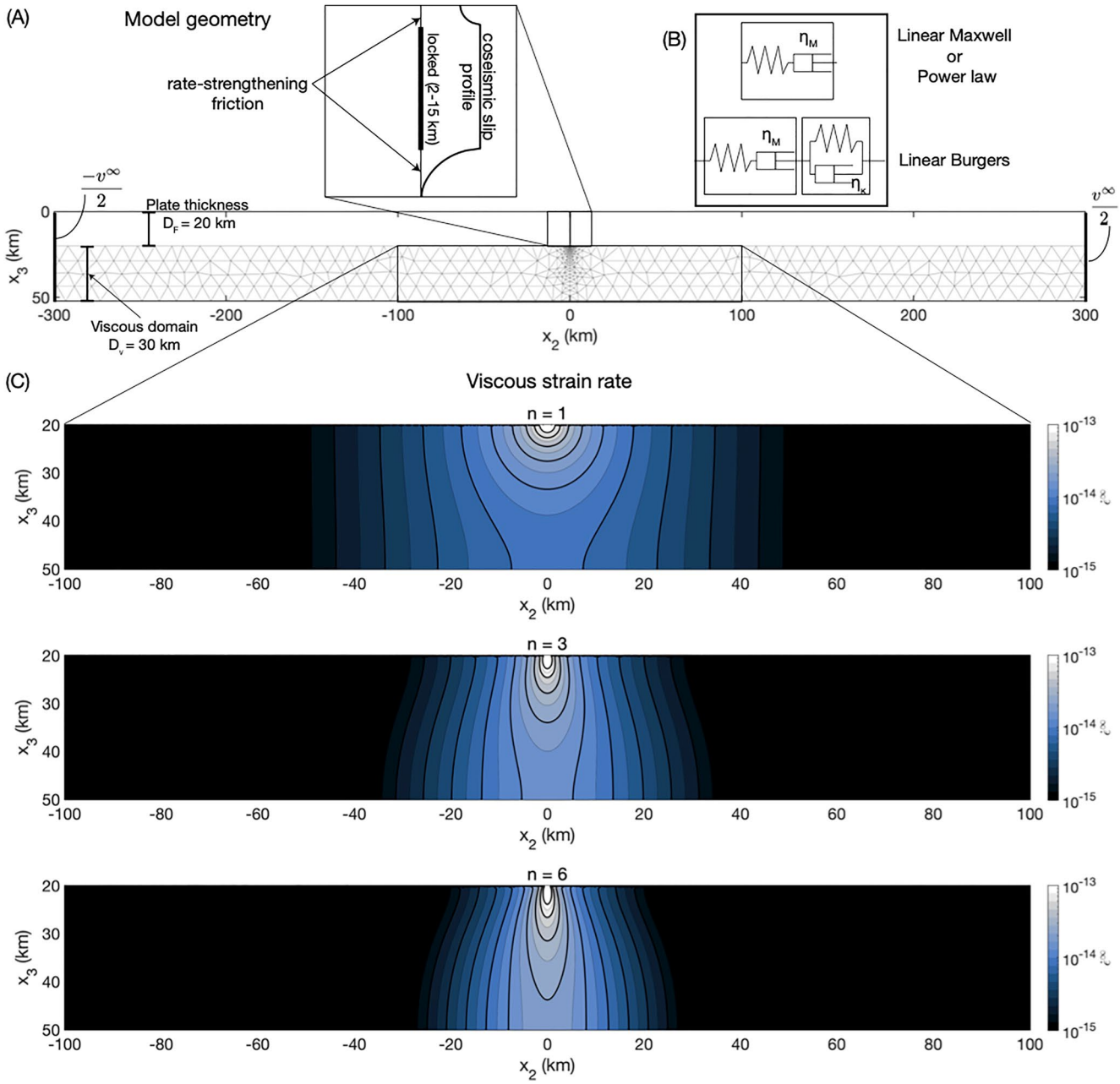

Figure 2. (a) Geometry of the numerical experiments. The domain of the stress calculations are separated into an elasto-frictional domain from 0 to 20 km depth and a viscoelastic domain from 20 to 50 km depth. Shear resistance in the frictional domain is given by rate-state friction, while the viscoelastic domain is governed by either a Maxwell rheology (the dashpot can be linear or power-law) or a linear Burgers rheology. (b) These rheologies are shown schematically. η_M—Maxwell viscosity, η_k—Kelvin viscosity. (c) Long-term viscous strain rate $\left(\sqrt{\left(\dot{\varepsilon}_{12}^{\infty}\right)^2+\left(\dot{\varepsilon}_{13}^{\infty}\right)^2}\right)$ as a function of the power exponent n.

in the crust (quartz) and mantle (olivine) (Hirth, 2002; Hirth & Kohlstedt, 2003). These flow laws are then evaluated at values determined from geological estimates of compositional and thermal variations within the lithosphere to derive rock rheologies at the kilometer scale (Lyzenga et al., 1991; Reches et al., 1994; Takeuchi & Fialko, 2012, 2013). Recent numerical studies have incorporated viscoelastic deformation in simulations of earthquake sequences along a strike-slip fault setting, providing a self-consistent framework that can reproduce all aspects of the earthquake cycle, including spontaneous earthquake nucleation, propagation, and arrest (Allison & Dunham, 2017, 2021; Lambert & Barbot, 2016).

Both classes of numerical simulations pose their own challenges. Linear viscoelastic models are borne out of computational simplicity and are able to fit many aspects of postseismic deformation, however, they predict late interseismic locking depths that are significantly deeper than the brittle-ductile transition and are limited in their ability to match observations (e.g., Takeuchi & Fialko, 2012). Numerical simulations that make use of more sophisticated laboratory-derived flow laws are more numerically challenging and computationally expensive (e.g., Lambert & Barbot, 2016). While they are able to better explain observations over the entire period between earthquakes, their relatively high computational expense poses a challenge for coupling them into an observational data-driven optimization problem, limiting their current utility for exploring and identifying effective constitutive relations of the lithosphere. Thus, there is need for a class of simulations that both satisfies the plate motion-derived kinematic boundary conditions and enables efficient exploration of various rheological parameterizations in order to evaluate what constraints may be afforded from surface deformation data on the effective rheology of the lithosphere.

1.4. Aim of This Study

In this article, we examine the use of earthquakes and the related cycle of loading and stress release, in an idealized two-dimensional strike-slip fault geometry, to study the rheological properties of the lithosphere. We develop numerical models of periodic earthquake cycles that can handle all popularly employed rheological models, satisfy the applied boundary conditions in the long-term (integrated over many earthquake cycles) as well as mechanical equilibrium throughout the earthquake cycle, and still remain computationally inexpensive.

We qualitatively compare the predictions from our simulations with observations from strain-rate regimes that are orders of magnitude apart, that is, the interseismic period ($\dot{\epsilon} < \dot{\epsilon}^{\infty}$) and the postseismic period ($\dot{\epsilon} \geq 10\dot{\epsilon}^{\infty}$), where $\dot{\epsilon}^{\infty}$ refers to the steady-state strain rate of the system or the strain rate averaged over geological timescales ($\sim$1 Ma). We do not attempt to solve for a best-fit rheological description like one would in an inverse problem sense. Instead, we show that linear viscoelastic rheologies need different parameters to explain the interseismic and postseismic periods of the earthquake cycle, as can be modeled by a Burgers rheology (e.g., Hearn & Thatcher, 2015), while steady state power-law rheologies with power exponent $n \geq 3$ are able to simultaneously explain the observed localization of strain preceding great earthquakes on mature faults, as well as the typical curvature observed in postseismic deformation time series. Discriminating between Burgers and steady state power-law rheological models using a single earthquake cycle may not be possible using available geodetic time series. However, we discuss how this task may become significantly more feasible if we include observations over sequences of earthquakes, particularly of different earthquake size.

2. Methods

Our numerical model is developed in an anti-plane geometry, that is, displacements are only in the out-of-plane x_1 direction, while displacement gradients exist in the $x_2 \times x_3$ plane. We consider a faulted elastic plate supported by a visco-elastic substrate subject to imposed boundary conditions. The thickness of the elastic plate is D_{F}, while the viscous substrate extends from (D_{F}, $D_{\mathrm{F}} + D_{\mathrm{V}}$). The elastic plate extends infinitely in the x_2 direction, and the viscous domain is chosen to be large enough to approximate this infinite x_2 extent (Figure 2a).

We first solve the viscous boundary-value problem for the long-term simulation and obtain the inelastic strain rate and slip rate of the viscous medium and fault, respectively. We combine these long-term rates with an elasticity kernel to formulate a set of Boundary Integral Equations to simulate the earthquake cycle (Mallick et al., 2021).

2.1. Long-Term Viscous Strain Rate

The governing equation for the viscous boundary-value problem is posed in terms of the scalar velocity field $v(x_2, x_3)$,

$$\nabla^2 v(x_2, x_3) = -\left(\frac{\partial \log \eta}{\partial x_2} \frac{\partial v(x_2, x_3)}{\partial x_2} + \frac{\partial \log \eta}{\partial x_3} \frac{\partial v(x_2, x_3)}{\partial x_3} \right) \tag{1}$$

where rheology of the substrate is described as follows,

$$\frac{1}{\eta} = A\left(\sqrt{\sigma_{12}^2 + \sigma_{13}^2} \right)^{n-1}; \quad \sigma_{1i} = \eta \dot{\epsilon}_{1i} = \eta \left(\frac{1}{2} \frac{\partial v}{\partial x_i} \right) \tag{2}$$

A is a rheological constant, n is the power in the power-law relation $\dot{\varepsilon} = A\sigma^n$, η is the viscosity, and the individual stress components are σ_{1i}.

2.1.1. Boundary Conditions and Solution

The boundary conditions on this system are as follows: traction-free at the base ($\sigma_{13}\,(x_3 = D_F + D_V) = 0$); lateral edges are subject to anti-symmetric Dirichlet boundaries $\left(v\,(x_2 \to \pm\infty) = \pm\frac{v^\infty}{2}\right)$; the entire fault slips uniformly at v^∞ resulting in rigid block-like motion of the elastic layer ($0 \le x_3 \le D_F$).

There exist analytical solutions to this system, at least for spatially uniform values of A, n (Moore & Parsons, 2015). The viscous strain rates for a choice of power-law rheology only depend on n (Figure 2c) and weakly depend on the dimensions of the system. We present these solutions in terms of rescaled dimensions x_2', x_3', where $x_3' = \frac{x_3 - D_F}{D_V}$ and $x_2' = \frac{x_2}{D_V}$. The domain for the solutions are $0 \le x_3' \le 1, -\omega \le x_2' \le \omega$. We choose the aspect ratio $\omega = 10$, which is sufficiently large such that there are negligible effects due to the location of the boundary on the strain-rate tensor (Moore & Parsons, 2015).

$$\begin{aligned}\frac{\dot{\varepsilon}_{12}^{\infty}}{v^{\infty}} &= \frac{1}{2\omega} + \frac{1}{\omega}\left(\sum_{m=1}^{\infty} \frac{\cosh\frac{m\pi\left(1-x_3'\right)}{\omega\sqrt{n}}}{\cosh\frac{m\pi}{\omega\sqrt{n}}} \cos\frac{m\pi x_2'}{\omega\sqrt{n}}\right)\\ \frac{\dot{\varepsilon}_{13}^{\infty}}{v^{\infty}} &= -\frac{1}{\omega\sqrt{n}}\left(\sum_{m=1}^{\infty} \frac{\sinh\frac{m\pi\left(1-x_3'\right)}{\omega\sqrt{n}}}{\cosh\frac{m\pi}{\omega\sqrt{n}}} \sin\frac{m\pi x_2'}{\omega\sqrt{n}}\right)\end{aligned} \tag{3}$$

We remind the reader that $\dot{\varepsilon}$ refers exclusively to the viscous component of the strain rate. The total strain rate, which is a sum of the viscous and elastic components, is denoted as $\dot{\varepsilon}_{\text{total}} = \dot{\varepsilon} + \dot{\varepsilon}_{\text{elastic}}$.

2.2. Periodic Earthquake Cycle Simulations

The steady-state solutions for long-term viscous creep rate (Equation 3, Figure 2c) can be used to compute an equivalent background stressing rate to load earthquake cycle simulations (Mallick et al., 2021). We note that without the long-term strain rates, one would have to assign a spatially variable long-term slip rate and strain rate to drive the earthquake cycle simulations (e.g., Lambert & Barbot, 2016), but this would not necessarily satisfy the boundary conditions of the system.

Using a background stressing rate that is kinematically and dynamically consistent with the long-term boundary conditions, we transform the time-dependent partial differential equations for quasi-static equilibrium to a set of coupled ordinary differential equations (e.g., Lambert & Barbot, 2016; Mallick et al., 2021). Here we discuss the procedure in brief; we discretize the nonelastically deforming part of the domain using constant-slip boundary elements for faults and constant-strain boundary elements for viscous shear. These boundary elements along with Equation 3 can be used to compute the long-term loading rate of the system as follows,

$$\begin{bmatrix}\dot{\sigma}_F^{\infty}\\ \dot{\sigma}_{12}^{\infty}\\ \dot{\sigma}_{13}^{\infty}\end{bmatrix} = \begin{bmatrix}K_{F,F} & K_{F,12} & K_{F,13}\\ K_{12,F} & K_{12,12} & K_{12,13}\\ K_{13,F} & K_{13,12} & K_{13,13}\end{bmatrix}\begin{bmatrix}-v^{\infty}\\ -\dot{\varepsilon}_{12}^{\infty}\\ -\dot{\varepsilon}_{13}^{\infty}\end{bmatrix} \tag{4}$$

$K_{a,b}$ is a stress-interaction kernel or the boundary-element approximation of the Green's function tensor that describes the elastic stress transfer to any given element a in response to inelastic shear (slip on faults and strain in shear zones) on the considered element b (Barbot, 2018).

Deviations from the long-term loading rate (Equation 4) drive frictional slip and viscous shear within the computational domain over the earthquake cycle. The set of coupled ordinary differential equations we need to solve is therefore the instantaneous momentum balance for each boundary element (e.g., Mallick et al., 2021). To do this,

Table 1
Model Parameters for Earthquake Cycle Simulations

Parameter	Range
Fault width	20 km
x_3 scale	30 km
x_2 scale	200–500 km
Shear modulus (G)	30 GPa
T_{eq}	50, 100, 200 years
v^{∞}	10^{-9} m/s
Viscous layer (linear Maxwell, power-law)	
Δx	Variable mesh size
n	1, 2, 3, 4, 5, 6
A^{-1}	10^{18}, 3×10^{18}, 7×10^{18}, 10^{19}, 5×10^{19}, 10^{20}
Viscous layer (linear Burgers)	
Δx	Variable mesh size
η_M (Pa-s)	10^{18}, 5×10^{18}, 10^{19}, 5×10^{19}, 10^{20}
η_k (Pa-s)	5×10^{17}, 10^{18}, 5×10^{18}
Fault parameters	
Δx_3	500 m
$a-b$	0.005
σ_n	50 MPa
f_0, v_0	0.6, 10^{-6} m/s

we account for the full elastic interaction between each point on the fault and in the viscous shear zones using the above described stress interaction kernel.

$$\begin{bmatrix} K_{F,F} & K_{F,12} & K_{F,13} \\ K_{12,F} & K_{12,12} & K_{12,13} \\ K_{13,F} & K_{13,12} & K_{13,13} \end{bmatrix} \begin{bmatrix} v - v^{\infty} \\ \dot{\epsilon}_{12} - \dot{\epsilon}^{\infty}_{12} \\ \dot{\epsilon}_{13} - \dot{\epsilon}^{\infty}_{13} \end{bmatrix} = \begin{bmatrix} \frac{\mathrm{d}\sigma_{\text{friction}}}{\mathrm{d}t} \\ \dot{\epsilon}_{12}\frac{\mathrm{d}\eta}{\mathrm{d}t} + \eta\frac{\mathrm{d}\dot{\epsilon}_{12}}{\mathrm{d}t} \\ \dot{\epsilon}_{13}\frac{\mathrm{d}\eta}{\mathrm{d}t} + \eta\frac{\mathrm{d}\dot{\epsilon}_{13}}{\mathrm{d}t} \end{bmatrix} \quad (5)$$

The left-hand side of this set of equations is the stressing rate in the system arising from elasticity while the right-hand side is the time derivative of the shear resistance provided by the rheology of the fault zone and viscoelastic medium. Details about the chosen rheologies are provided in the following section.

2.2.1. Friction and Viscous Laws

Resistive strength evolution on the fault (Equation 5) is described by rate-dependent friction (Marone et al., 1991), that is, the resistive strength of the fault is given by $f\sigma_n$ where f is the friction coefficient and σ_n is the effective normal strength on the fault, and reference values f_0, v_0.

$$\sigma_{\text{friction}} = f(v)\sigma_n = \left(f_0 + (a-b)\log\frac{v}{v_0}\right)\sigma_n \quad (6)$$

The values for each parameter is shown in Table 1, and are only applicable to the regions where postseismic creep can occur, that is, between 0–2 and 15–20 km on the fault (Figure 2a).

The rheological models we test in the viscoelastic domain are the linear Maxwell, linear Burgers, and power-law rheologies (Figure 2b). The total strain rate in these rheologies are of the form,

$$\dot{\varepsilon}_{\text{total}} = \frac{\dot{\sigma}}{G} + \frac{\sigma}{\eta_M} + \dot{\varepsilon}_k \begin{cases} \frac{\sigma - G\varepsilon_k}{\eta_k}, & \text{Burgers body} \\ 0, & \text{otherwise} \end{cases} \quad (7)$$

where $\dot{\varepsilon}_k$ is the Kelvin strain only present for a Burgers body, η_{M} is the viscosity of the Maxwell element (for power-law rheologies, η_{M} in turn is a function of ε, i.e., $\frac{\mathrm{d}\eta}{\mathrm{d}t} \neq 0$ in Equation 5) and G is the elastic shear modulus of the system.

To study the role of viscous rheology in modulating the stress state in this system, and the associated displacement and velocity field at the free surface, we vary the two parameters used to describe the rheology in the viscous shear layer for the spring-dashpot bodies (linear Maxwell and power-law): A, n; while we vary the Kelvin and Maxwell viscosities for the Burgers material: η_k, η. We also vary the recurrence time for the earthquake to see how relaxation in the lithosphere is related to the magnitude of coseismic stress perturbation. We list model parameters we varied for these simulations in Table 1.

2.2.2. Initial Conditions From Coseismic Slip

The set of ordinary differential equations we need to solve is Equation 5 in terms of the variables $[v, \dot{\epsilon}_{12}, \dot{\epsilon}_{13}]$, subject to the rheologies in Equations 6 and 7. To guarantee a unique solution for this system, we need to determine the initial condition for $[v, \dot{\epsilon}_{12}, \dot{\epsilon}_{13}]$. This is done by using the stress change due to prescribed coseismic slip on the fault to instantaneously change values of $[v, \dot{\epsilon}_{12}, \dot{\epsilon}_{13}]$ subject to their rheological properties.

We prescribe coseismic slip as a uniform value of $u^{\infty} = v^{\infty}T_{eq}$ within the locked domain ($2\text{ km} \leq x_{co} \leq 15\text{ km}$), and tapered in the surrounding section of fault ($0\text{ km} \leq x_{as} \leq 2\text{ km} \cup 15\text{ km} \leq x_{as} \leq 20\text{ km}$) such that the stress increase does not exceed 3 MPa and slip within this domain is minimized (Figure 2a). The stress change calculations only require the previously computed Green's function tensor for elastic stress interactions K,

$$K_{x_{as},x_{co}} u^{\infty}(x_{co}) + K_{x_{as},x_{as}} \Delta u^{\infty}(x_{as}) \leq 3\text{MPa}$$
$$\Delta u^{\infty}(x_{as}) \sim 0 \tag{8}$$

where $u^{\infty}(x_{co})$ is uniform slip applied within the locked domain and $\Delta u^{\infty}(x_{as})$ is the tapered slip within the rate-strengthening frictional domain. This is a linear inequality constrained optimization for $\Delta u^{\infty}(x_{as})$ that is done using the MATLAB function *lsqlin*. The resulting shape of this profile on the fault is shown in Figure 2a.

With the initial conditions determined from coseismic slip, we integrate the system of equations using MATLAB's Runge-Kutta fourth order solver *ode45* to obtain the time history of fault velocity (within the rate-strengthening domain) and viscous strain rates $[v, \dot{\epsilon}_{12}, \dot{\epsilon}_{13}]$ over the entire domain. Since the coseismic slip derived initial conditions only provide a change in the integrable variables, we need to run these earthquake cycles a number of times until we obtain cycle invariant results (e.g., Hetland & Hager, 2005; Takeuchi & Fialko, 2012). In that case, the coseismic slip-derived stress change is imposed every T_{eq} years. We find that, depending on rheology, 10–20 cycles is sufficient to obtain cycle invariant results given the rheological parameters and timescales we have chosen.

2.3. Parameters That Can Be Estimated Geodetically

The earthquake cycle simulations give us the time history of fault slip rate and viscous strain rates within the viscoelastic medium, which we then combine with displacement Green's functions to predict displacement time series at the free surface (Barbot, 2018). Since our focus in this article is the behavior of the viscoelastic domain, we neglect the fault slip rate evolution in the predicted surface deformation time series. We consider two main parameters that can be inferred geodetically that are generally used to describe the period following and leading up to large plate boundary earthquakes. In the postseismic period, we estimate the effective relaxation time of the system, t_R; we describe the interseismic signal using an effective locking depth, D_{lock}.

For postseismic relaxation, we consider only the deviation from steady state behavior, that is, we remove displacements associated with the long-term motion of the plate boundary or the steady-state strain rates $\left(\dot{\epsilon}_{12}^{\infty}, \dot{\epsilon}_{13}^{\infty}\right)$. We characterize the transient surface displacements during the first 2 years following the earthquake using a two-step procedure. First, we use singular-value decomposition on the displacement time series and extract the temporal component associated with the most dominant singular value. We fit this with the following functional form,

$$u(t) = \beta \left(1 - \exp\left(\frac{-t}{t_R}\right)\right). \tag{9}$$

β, t_R are estimated using a MATLAB-based nonlinear least squares routine, and t_R gives the best-fit relaxation time of the system over the observational window.

Later in the earthquake cycle, we consider the interseismic period as the time period when the maximum surface velocity is smaller than the relative plate velocity, that is, $|v(x_2)| \leq \frac{v^{\infty}}{2}$. The resulting velocity field can then be fit to an arc-tangent function (Savage & Burford, 1973),

$$v(x_2) = \frac{v^{\infty}}{\pi} \tan^{-1}\left(\frac{x_2}{D_{lock}}\right). \tag{10}$$

The estimated locking depth controls the effective width of the surface that is experiencing interseismic strain, and is thus a physically motivated representation of the spatial pattern of the signal.

3. Results

We describe the surface deformation observations predicted at geodetic sites over the entire earthquake cycle, as well as the corresponding strain rate evolution within the viscoelastic domain from our numerical experiments (Figures 3 and 4). Since we are interested in cycle invariant behavior, we only present results from the last earthquake cycle; the previous cycles are necessary only for spin up. The results are discussed separately for linear Maxwell, linear Burgers, and power-law rheologies in terms of interseismic locking depths (Figure 5), cumulative postseismic displacements (Figure 6), and effective relaxation timescales (Figure 7). We note that our simulations allow for the mechanical coupling between frictional afterslip on the fault and

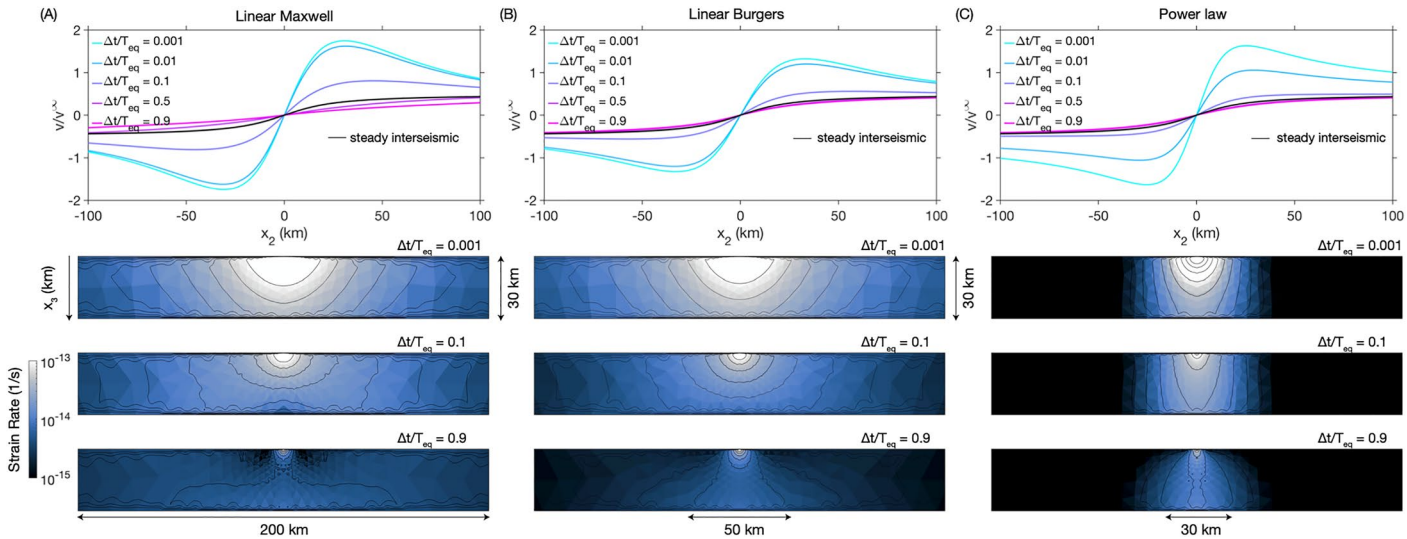

Figure 3. Surface velocity and internal viscous strain rate evolution over the earthquake cycle for different rheologies for a periodic earthquake cycle of $T_{eq} = 50$ years. The rheologies were chosen such that the early postseismic surface velocity field is nearly identical. (a) Linear Maxwell body ($\eta_M = 3 \times 10^{18}$ Pa-s), (b) Linear Burgers body ($\eta_k = 3 \times 10^{18}$ Pa-s, $\eta_M = 5 \times 10^{19}$ Pa-s), and (c) Power law rheology ($A^{-1} = 3 \times 10^{18}$, $n = 3$). The linear rheologies allow accelerated viscous deformation of significantly larger volume of material compared to the power-law rheology, which promotes localization of strain. This effect is noticeable in all the strain rate snapshots.

viscous creep in the viscoelastic domain. However, since our focus is on the behavior of the viscoelastic medium, the surface displacement and velocities that we discuss in subsequent sections do not contain contributions from afterslip.

3.1. Linear Maxwell

For linear Maxwell rheologies, both the amplitude and effective relaxation timescale of the postseismic response directly depend on the viscosity (η_M). As η_M increases, the timescale for stress relaxation following the coseismic perturbation (t_R) increases, while the magnitude of the initial jump in strain rate ($\Delta\dot{\epsilon}(\Delta t = 0)$) decreases.

$$t_R = \frac{\eta_M}{G}$$
$$\Delta\dot{\epsilon}_M(\Delta t = 0) = \frac{\Delta\tau_{co}}{\eta_M} \approx \frac{K\,(v^{\infty} T_{eq})}{\eta_M} \tag{11}$$

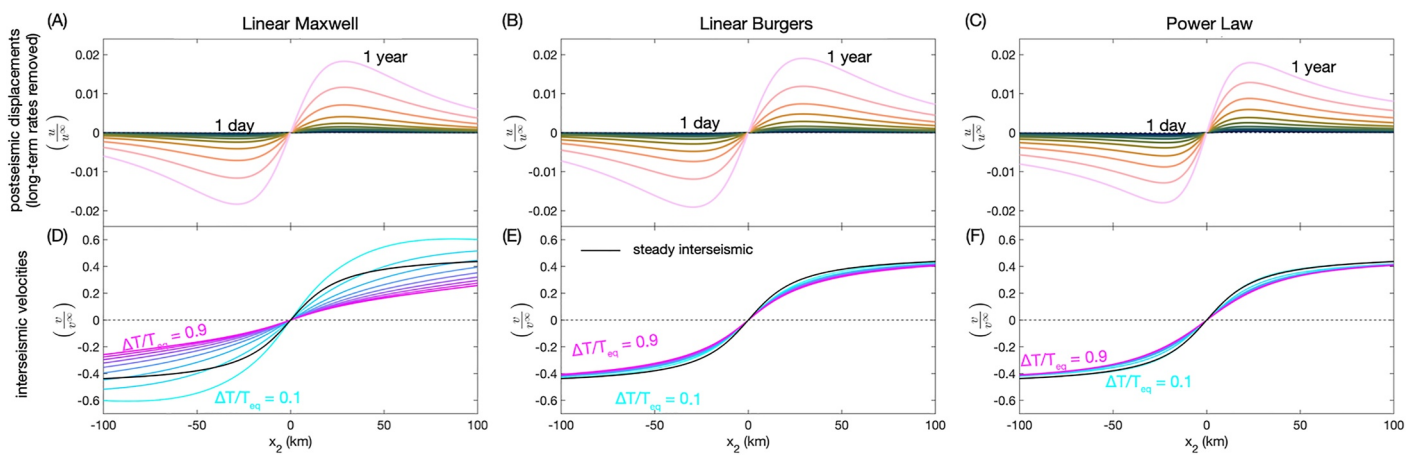

Figure 4. Surface predictions of postseismic displacements and interseismic velocities for different rheologies for a periodic earthquake cycle of $T_{eq} = 100$ years. The rheologies are chosen such that the cumulative postseismic after 1 year is nearly identical for all three models. (a)–(c) Cumulative postseismic displacements normalized by the coseismic slip amount $\left(u^{\infty} = v^{\infty} T_{eq}\right)$ for times varying from 1 day to 1 year. (d)–(f) Interseismic velocities compared to the steady interseismic expectation (black line).

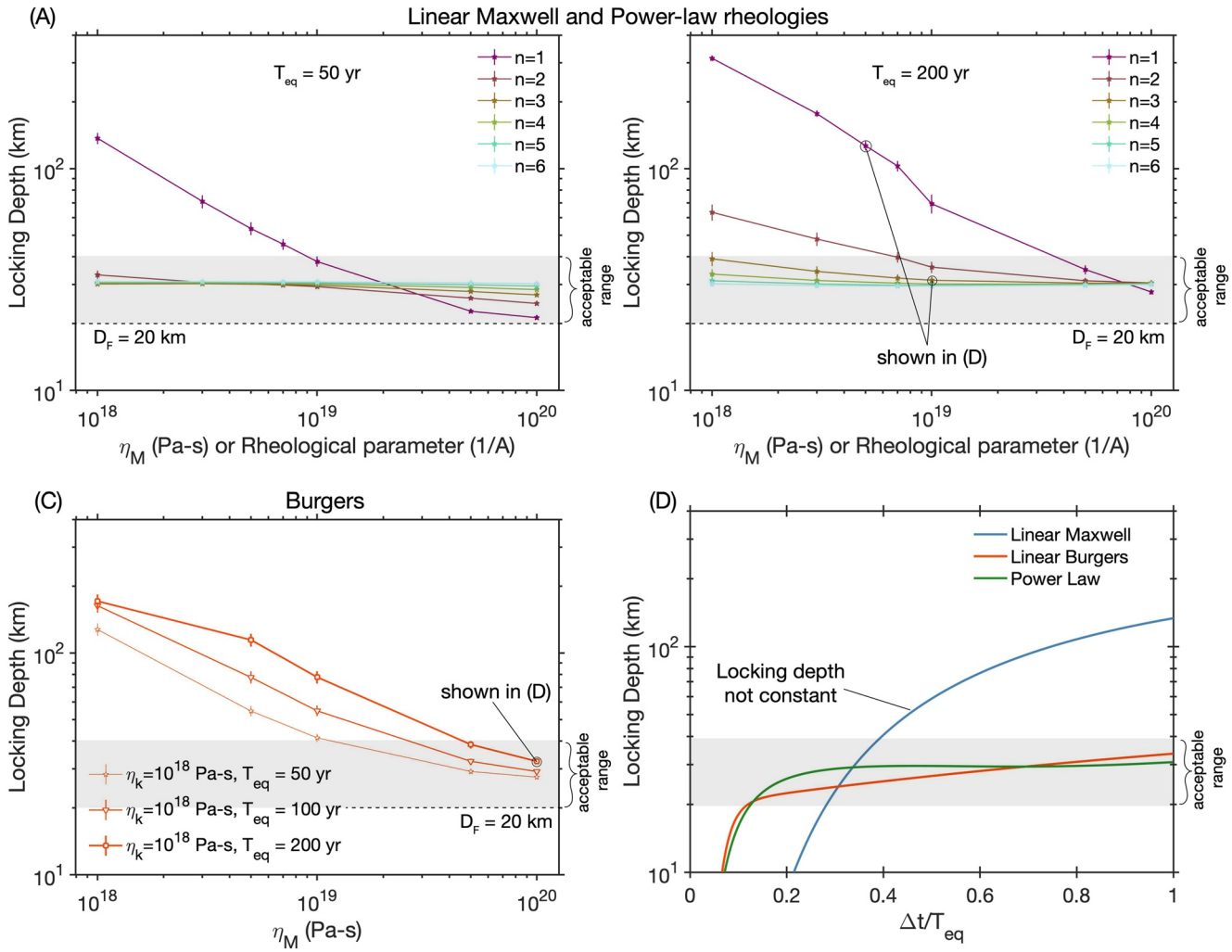

Figure 5. Compilation of late interseismic locking depths for various rheological choices and two different T_{eq}. Locking depth (assuming an arc-tangent functional fit—$\frac{\upsilon^{\infty}}{\pi}\tan^{-1}\frac{x_2}{D}$) for (a) Linear Maxwell and power-law materials with n varying from 1 to 6 for $T_{eq} = 50$ years. (b) Same as (a) for $T_{eq} = 200$ years. (c) Locking depths for a linear Burgers rheology for a constant η_k and varying η_M and T_{eq}. Late interseismic locking depths show no dependence on η_k. (d) The estimated locking depth varying in time over the interseismic period for different rheologies. Both the power-law body and linear Burgers (with large η_M) show nearly time invariant late-interseismic locking depth.

A dominant feature from simulations incorporating a linear Maxwell rheology is that they show strain rates that are diffusive is space and in time (Figure 3a). The initial strain rate following the earthquake decays in space as expected from the stress change $\Delta\tau_{co}$. In time, the elevated strain rate is damped as it diffuses outwards. At the end of the earthquake cycle ($\Delta t/T_{eq} \rightarrow 1$), nearly the entire viscoelastic medium is at a uniform strain rate level and the resulting surface velocity field appears to have a near constant spatial gradient (Figure 4d).

Many aspects of the evolution of this viscoelastic system can be explained by a single dimensionless variable, $\alpha_M = \frac{T_{eq}}{2t_R} = \frac{GT_{eq}}{2\eta_M}$ (Savage, 2000; Savage & Prescott, 1978). Models with $\alpha_M \gg 1$, in our simulations this mainly arises from low η_M, generate relatively large magnitude postseismic deformation early in the earthquake cycle (Figure 6) and predict relatively small near fault velocity gradients late in the earthquake cycle (Figures A3, 5d). Conversely, if $\alpha_M \ll 1$ or η_M is large, the system response approaches the elastic limit where there is negligible viscous response and the predicted surface velocities vary only moderately around the steady state elastic expectation throughout the earthquake cycle (Figures A3, 5a, 5b).

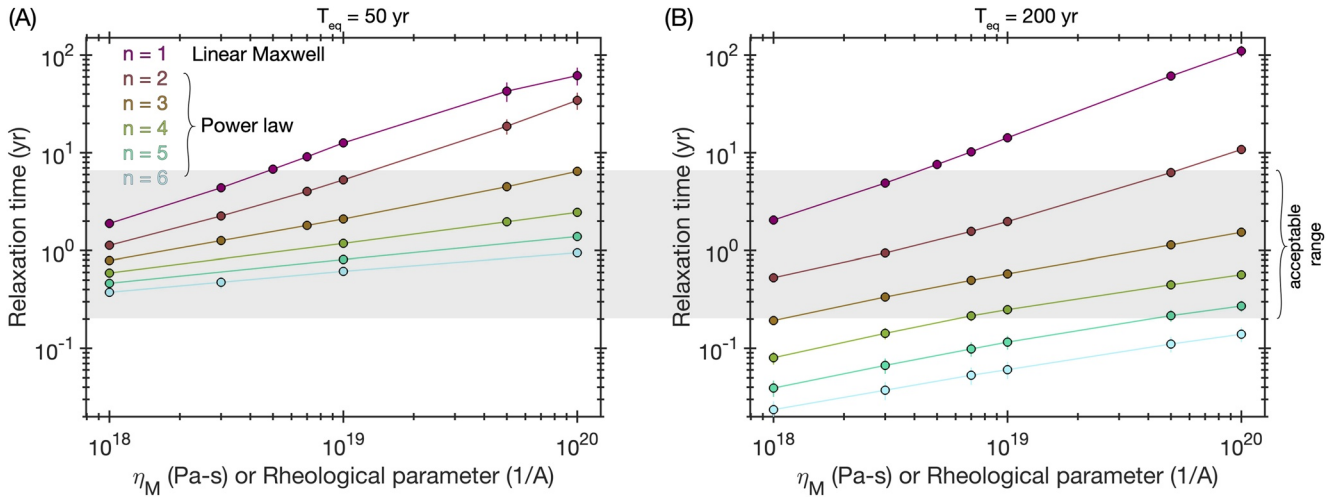

Figure 6. Postseismic relaxation times for linear Maxwell and power law bodies estimated over a 2-year period following the earthquake for a recurrence interval of (a) 50 years and (b) 200 years. Increased T_{eq} leads to larger coseismic slip $(u^{\infty} = v^{\infty} T_{eq})$, and hence larger stress change to drive postseismic creep. Linear Maxwell bodies follow a stress-independent relaxation time given by $t_R \approx \frac{\eta_M}{G}$. The relaxation time of power law bodies show a significant reduction for larger coseismic slip. We do not show the results for Burgers bodies, since their relaxation times over the given time window are exactly as predicted by the viscosity of the Kelvin element $t_R \approx \frac{\eta_k}{G}$.

3.2. Linear Burgers

The linear Burgers rheology is characterized by two separate timescales: a short-term anelastic timescale $\frac{\eta_k}{G}$ controlled by the viscosity of the Kelvin element, and a long-term Maxwell timescale $\frac{\eta_M}{G}$ (assuming $\eta_k < \eta_M$) (Hetland & Hager, 2005; Müller, 1986). Only the creep associated with the Maxwell element is recorded as permanent strain, the anelastic term is significant for geodetic observations but does not leave a record in the long-term.

Similar to the linear Maxwell case, the linear Burgers body also exhibits a tendency to diffuse strain rate away from the fault with time (Figure 3c). This pattern depends on three variables—T_{eq}, and the two relaxation times associated with η_k and η_M. Large values of η_k, η_M and small values of T_{eq}, lead to small stress perturbations and hence minimal deviation from a time-invariant steady-state model. Small values of η_k and η_M, or large values of T_{eq} lead to more pronounced earthquake cycle effects.

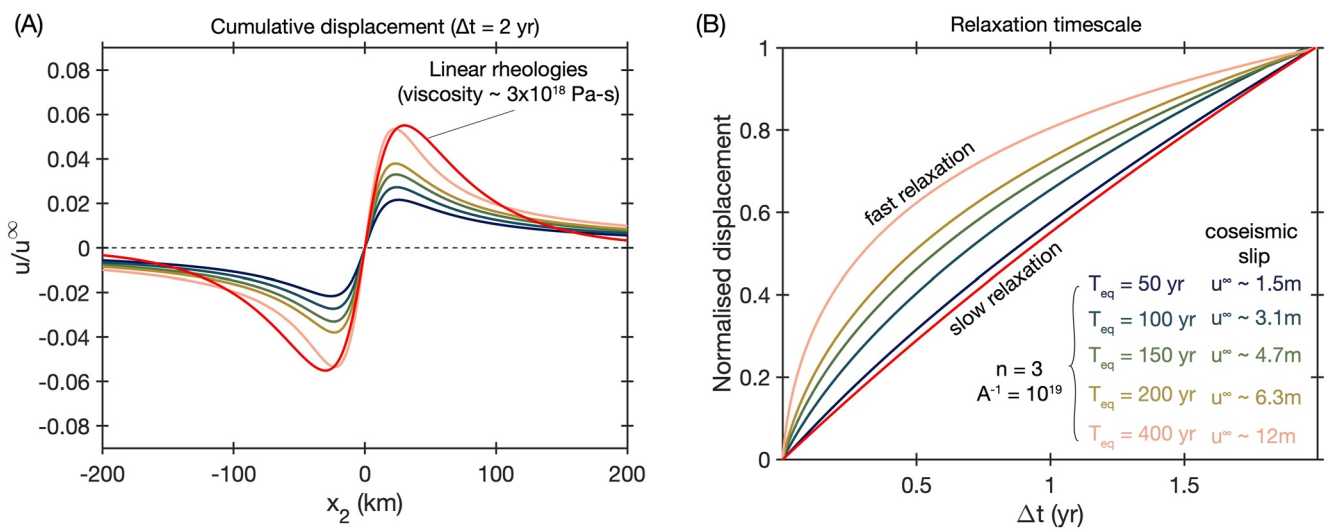

Figure 7. Magnitude dependent postseismic motions for power law bodies. (a) Cumulative postseismic displacement (steady state component removed) normalized by the coseismic slip amount $(u^{\infty} = v^{\infty} T_{eq})$ over 2 years for the same rheology. By increasing the earthquake recurrence interval, we increase the coseismic slip amount. Only power law materials show increasing cumulative deformation with increase in the recurrence interval. (b) As the cumulative deformation increases, the relaxation timescale decreases, that is, the postseismic deformation becomes faster and larger.

3.2.1. Interseismic Locking Depth

Late interseismic locking depths show systematic dependence on only two parameters—η_M and T_{eq} (Figure 5c). This indicates that for the parameter range we explore here, the late interseismic behavior is effectively controlled by the dimensionless variable, α_M which we discussed in the linear Maxwell case. Thus, small α_M values (large η_M) result in locking depth estimates comparable to purely frictional-elastic simulations (Figure 5d).

3.2.2. Postseismic Creep and Relaxation Time

Linear Burgers bodies do not have a single relaxation timescale, and thus our estimates of t_R depend on the time window that is considered. We consider a 2-year time window, which is a typical observational window used in geodetic studies, in order to estimate the relaxation time and effective viscosity of the system. In most of our simulations, this estimated relaxation time corresponds to sampling the viscous relaxation controlled by η_k (see caption in Figure 6).

3.3. Power-Law

Our numerical experiments governed by power-law rheologies are characterized by two main features—(a) the interseismic locking depths appear to be a constant in time and only weakly sensitive to the parameters we varied (Figures 5a and 5b), and (b) the postseismic relaxation timescale and amplitude appear to depend on the coseismic slip amplitude and conform poorly to the $\exp(-t/t_R)$ functional form we chose to fit it with (Figures 4c and 7b), that is, the curvature in the timeseries is closer to a logarithmic decay than the exponential function we chose (e.g., Montési, 2004).

3.3.1. Localized Deformation and Interseismic Locking Depth

For our simulations with power-law rheologies, deformation throughout the entirety of the earthquake cycle is significantly more localized in space than as observed for the linear viscoelastic rheologies discussed above (Figure 3c). The extent of localization depends on the power exponent n as well as the rheological parameter A. We contrast this with the fact that the solution to the long-term viscous boundary value problem does not depend on A (Equation 3). Thus, our simulation results suggest that both A and n may be inferred from geodetic data collected over the entire earthquake cycle.

Larger stress exponents n favor increased localization while large coefficients A reduce the impact of stress perturbations from coseismic slip, similar to how the magnitude of the viscosity of linear rheologies controls the change in strain rates in Equation 11. While the degree of strain localization depends on the power law stress exponent, for the parameter space explored, we find that models with power law exponents $n \geq 3$ exhibit nearly identical late interseismic locking depths (Figures 5a and 5d), and are generally comparable to simple back slip models of interseismically locked faults.

3.3.2. Postseismic Creep and Relaxation Time

The postseismic deformation time series is not expected to conform to the exponential functional form we used to fit the time series. This is because the exponential function is a solution to the linear viscoelastic problem, and the outputs of a power-law rheology correspond to an effective viscosity that systematically increases in time (Montési, 2004). However, since we consider time windows on the order of 1–2 years, the relaxation timescale can be fit using a linear viscoelastic approximation to estimate an average relaxation time over that window. These relaxation timescales are not only dependent on rheological parameters A, n but also are a function of the earthquake size, parameterized here in terms of coseismic slip (Figure 6).

For a given set of rheological parameters A, n (for $n > 1$), the cumulative postseismic deformation over a given time window (in this case $\Delta t = 2$ years), even when normalized by the coseismic slip amount, increases with earthquake size (Figure 7a). The normalized postseismic deformation following small earthquakes in our simulations ($u^{\infty} \sim$ 1.5 m) amounts to about 30% of the normalized postseismic deformation following the largest earthquakes ($u^{\infty} \sim$ 12m). On the other hand, the estimated relaxation timescale decreases with increasing earthquake size (Figure 7b).

4. Discussion

We have developed numerical earthquake cycle experiments in order to test how well popular rheological models are able to qualitatively reproduce different observational features in geodetic studies over the entire interseismic period. Our simulation results illustrate the nonuniqueness of rheological models, and their parameters, in explaining postseismic data alone (Figures 5–7).

Our simulations demonstrate that the nonuniqueness in interpreting postseismic data can to some extent be mitigated by incorporating data corresponding to strain accumulation in the late interseismic period (Figure 5). We find that steady-state power-law rheologies with $n \geq 3$ as well as linear Burgers rheology with $\eta_M \approx 10^{20}$ Pa-s and $\eta_k \approx 10^{18}$ Pa-s are able to explain early postseismic relaxation as well as the strain localization observed near strike-slip faults late in the interseismic period. While we do not show it explicitly, nonlinear Burgers rheologies with $n \geq 1$ (with relevant A values) could explain the geodetic data just as well. This is because a steady-state rheology, linear or power-law, is simply a limiting case of an appropriate Burgers rheology where the transient viscosity is much larger than the steady-state value. On the other hand, linear Maxwell rheologies are simply insufficient to explain the observational features.

In the following sections, we first discuss the equivalence between linear Burgers and power-law descriptions of lithospheric rheology for the earthquake cycle, and then detail geophysical observations that may be required to convincingly discriminate between these two rheologies. We then expound on the relationship between inferences of average rheological parameters from crustal scales and those measured in laboratory experiments, and how a power-law rheology is consistent with both geodetic observations and laboratory-derived flow laws. Finally, we conclude with the implications for stress transfer and the associated assessment of regional hazard when frictional and viscous creep are mechanically coupled.

4.1. The Effective Rheology of the Lithosphere

Geodetic investigations of lithospheric rheology, specifically the lower crust and uppermost mantle, that consider only a relatively short time window ($\Delta t < 5$ years) as is typical of geodetic postseismic studies, may not be able to distinguish between any of the rheological models discussed in this paper (linear Maxwell, linear Burgers, and power-law). This is because postseismic geodetic observations can be reduced to two features—a spatial pattern of cumulative postseismic deformation and the effective relaxation timescale (Figure 7), and there exists a nonunique mapping between rheological parameters from each of the discussed rheological models to these spatial and temporal patterns of the deformation data (Figures 7, 8a and 8b).

However, the three rheological models display diverging behavior as the observational window gets larger; this is what we exploit during the late interseismic period. Interseismic strain localization and the stationarity of the locking depth in time is observed in models with either a power-law rheology or a linear Burgers rheology that approximates the effective viscosity evolution of a power-law body (Figure 8d). In contrast, linear Maxwell rheologies promote diffuse strain distributions (Figure 3) which manifests as an increase in effective locking depths late in the earthquake cycle (Figure 5d), a feature that is not seen even in the best monitored strike-slip fault systems in the world (e.g., Hussain et al., 2018). This leads us to suggest that Earth's lithosphere cannot be well-described by a homogenous linear Maxwell body, at least over the timescale of the earthquake cycle.

These findings do not invalidate previous work on estimating the effective viscosity from postseismic, postglacial and lake rebound deformation observations assuming a linear Maxwell rheology (e.g., Devries & Meade, 2013; England et al., 2013; Johnson & Segall, 2004; Kaufmann & Amelung, 2000; Kenner & Segall, 2003; Larsen et al., 2005; Tamisiea et al., 2007). However, the important implication is that these estimates of the average viscosity, or viscosity structure, are tied to the observational window. This detail becomes apparent when comparing the lithospheric viscosities estimated from processes that occur over different timescales; longer observations windows typically show significantly higher viscosities, for example, the viscosity of the upper mantle estimated following deglaciation (since the Last Glacial Maximum), which represents a $\sim 10^4$ year observational time window, is between 10^{20} and 10^{21} Pa-s (e.g., Milne et al., 2001; Tamisiea et al., 2007) while typical viscosities estimated in the decade(s) following $M_w > 7$ earthquakes range from 10^{18} to 10^{19} Pa-s (e.g., Kenner & Segall, 2003; Pollitz, 2005; Ryder et al., 2007). Viscosities estimated nearly 50 years after the largest earthquakes in the 20th century appear to favor viscosities in the range $10^{19} - 10^{20}$ Pa-s (Freymueller et al., 2000; Khazaradze et al., 2002; Melnick et al., 2018; Suito & Freymueller, 2009). Both power-law and linear Burgers rheologies

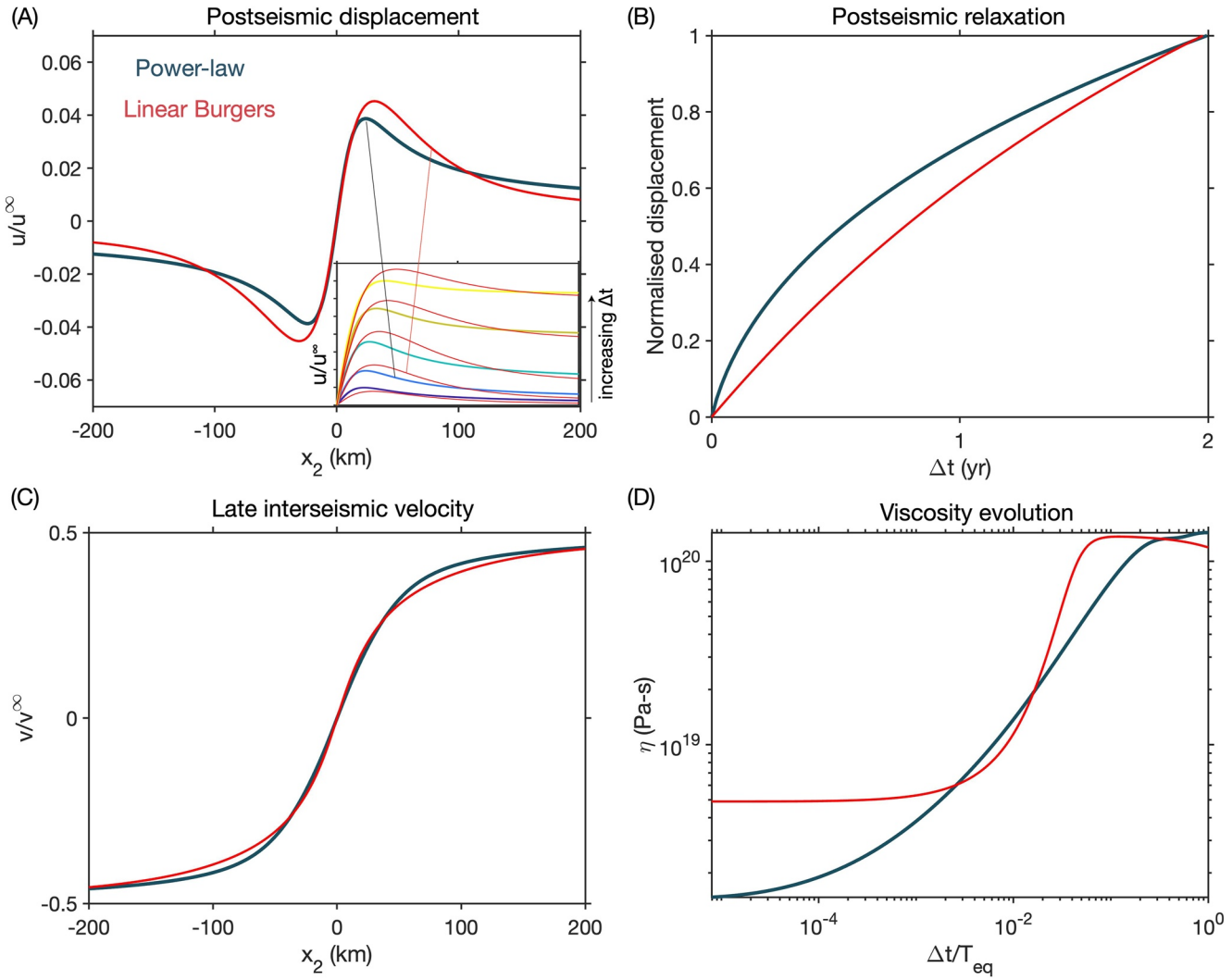

Figure 8. Approximating power-law rheology $(A = 10^{19}, n = 3)$ with a linear Burgers body ($\eta_M = 10^{20}$ Pa-s, $\eta_k = 3 \times 10^{18}$ Pa-s) for $T_{eq} = 200$ years. (a) Cumulative displacement for power-law and linear Burgers rheologies after 2 years. The inset shows snapshots of cumulative deformation over increasing time windows of 0.5, 2, 10, 30, 50 years (blue—short timescale, yellow—long timescale). (b) Relaxation time function extracted from the time series. (c) Late interseismic velocity field. (d) Average viscosity evolution in time for both rheological models. $\eta(\Delta t) = \frac{\iint \eta(x_2,x_3,\Delta t)|\dot{\varepsilon}(x_2,x_3,\Delta t)|dx_2dx_3}{\iint |\dot{\varepsilon}(x_2,x_3,\Delta t)|dx_2dx_3}$ where $|\dot{\varepsilon}| = \sqrt{\dot{\varepsilon}_{12}^2 + \dot{\varepsilon}_{13}^2}$.

can help reconcile these apparently disparate viscosity estimates, since both processes produce time-dependent viscosities which increase with time since the applied stress perturbation (Figure 8d).

4.1.1. Similarities Between Power-Law and Linear Burgers Rheologies

A question that arises at this point is—how can a linear and power-law rheology satisfactorily explain deformational data throughout the earthquake cycle? The near equivalence between linear Burgers and power-law bodies in our simulations exists because of a nonunique mapping between rheological parameters for each model and the observational features that we use to describe the deformation time series (Figures 8a–8c).

Consider the viscosity evolution of a power-law body. The power-law rheology results in a lower effective viscosity during the relatively high stress and strain rate postseismic period, and the viscosity gradually increases as stress relaxes and decays to a near time-invariant interseismic state (Figure 8d). The linear Burgers rheology captures this same kinematic behavior through completely different dynamics. The Burgers description can be thought of as a technique to describe nonsteady state viscous rheology, that is, there exists a finite timescale or strain over which the system has to evolve to reach the unique mapping between stress and strain rate (Hetland & Hager, 2005; Müller, 1986). In the case of a linear Burgers rheology, the initial low effective viscosity during

the postseismic period is a disequilibrium feature that smoothly evolves to its significantly larger steady state viscosity (Figure 8d).

While the overall kinematics predicted by the two different rheological models appear similar, the predictions from the two models are not identical (Figure 8a, inset). Although they would likely be difficult to distinguish after considering the errors and uncertainties in typical geodetic data sets and the various models employed to fit the data (Duputel et al., 2014; Minson et al., 2013).

4.1.2. Magnitude-Dependent Postseismic Motions

Our simulation results suggest that linear Burgers and power-law rheologies may in principle be distinguished by the sensitivity and rate of the postseismic moment release to the magnitude of the coseismic event. For a typical time window ($\Delta t = 2$ years), linear viscoelastic rheologies result in postseismic surface deformation that is a linear function of the coseismic slip $\left(u^{\infty} = v^{\infty} T_{\text{eq}}\right)$, and thus can be normalized to produce a constant shape (Figure 7a). Similarly, the temporal evolution of this moment release is invariant of the size of the earthquake (Figure 7b). In contrast, power-law rheologies show a clear magnitude dependence, where the normalized postseismic deformation at the surface is smaller for small events and grows larger with increasing coseismic slip (Figure 7a). The temporal evolution of moment release is also a function of event size with smaller events having much slower relaxation than larger events (Figure 7b).

While this magnitude-dependent behavior has not been studied thoroughly, there is some evidence to suggest the existence a magnitude-dependent pattern in postseismic observations, supporting the interpretation that lithospheric deformation may follow a power-law rheology. For example, multiyear postseismic viscoelastic deformation has been clearly observed and documented following $M_{\text{W}} > 7$ continental earthquakes (e.g., Freed & Bürgmann, 2004; Freed et al., 2010; Moore et al., 2017; Pollitz, 2019; Savage & Svarc, 2009; Tang et al., 2019; Wang & Fialko, 2018; Wen et al., 2012; Zhao et al., 2021), however, observations of notable viscoelastic deformation following slightly smaller ($6.5 < M_{\text{W}} < 7.0$) continental earthquakes are equivocal (e.g. Bruhat et al., 2011; Savage et al., 1998; Wimpenny et al., 2017). Such distinction in observed postseismic behavior for different sized earthquake ruptures may indicate a critical coseismic stress perturbation required to activate geodetically detectable viscous flow, as would be expected from power-law rheologies (Figure 7). Identifying a clear magnitude-dependence of postseismic viscous response may be challenging given the limited historical data available for individual fault segments, however, a careful global compilation of postseismic deformation over a fixed time window following strike-slip fault earthquakes ranging from M_w 6 to 8 may provide further insight to any systematic magnitude-dependent response, and help discriminate between rheological models of the lithosphere.

4.2. What do Estimates of A and n Mean at the Lithospheric Scale?

As previously discussed, geodetic data over a single earthquake cycle is consistent with two classes of rheological models: (a) steady-state flow laws with power law exponents $n \geq 3$ and a range of A values, and (b) an unsteady flow law with $n = 1$, $\eta_k/\eta_M < 0.1$, and $\eta_M \geq 10^{20}$ Pa-s. We note that for unsteady flow laws, we have only explicitly considered the linear Burgers rheology ($n = 1$); a power-law rheology with an additional unsteady or transient element can exactly reproduce the observations as well. The principle of parsimony would suggest that a steady-state power-law rheology presents a better representation of the lithosphere, but we turn to the literature from the mineral physics community to expound on the appropriate rheological choice as well as how to interpret what are effectively kilometer-scale averaged estimates of rheological parameters $\hat{A}$, $\hat{n}$ (and $\hat{\eta}_k$) from geodetic data.

There are two main aspects to this discussion—(a) the contribution of multiple different mechanisms to the inferred parameters $\left(\hat{A}, \hat{n}, \hat{\eta}_k\right)$, and (b) the spatially heterogeneous variations of the parameters of various mechanisms to our spatially uniform estimates of the inferred rheological parameters.

4.2.1. Averaging Over Multiple Mechanisms and Assemblages

The simplified rheology we employ in this article (Equation 2) is a composite flow law, that under the assumption of linear mixing would attempt to approximate a linear combination of multiple microscale processes in the following way,

$$\dot{\varepsilon} = \hat{A}\sigma^{\hat{n}} \approx \sum_i \left[c_i \exp\left(-\frac{Q_i + PV_i^*}{RT} \right) d^{-m_i} C_{\text{fluid}}^{r_i} \right] \sigma^{n_i} \quad (12)$$

This summation indicates simultaneously active processes with different values of the power-law exponent (n_i), each having material specific corresponding activation energy and volumes $\left(Q_i, V_i^*\right)$, grain size dependence (m_i) and fluid phase dependence (r_i). c_i is a material and process-specific constant, C_{fluid} may refer to either the water fugacity or melt fraction, R is the universal gas constant, T is the absolute temperature of the system, and d is a central tendency of the grain size distribution in the sample.

Power-law rheologies for rocks with stress exponents of $n \sim 3$–4 are considered representative of dislocation creep, where deformation is accommodated by the migration of dislocations and dislocation planes within the crystal lattice (e.g., Chopra & Paterson, 1981; Hirth & Kohlstedt, 2003); linear rheologies indicate the diffusion of vacancies and defects through the mineral grains and grain boundaries (e.g., Karato et al., 1986; Rutter & Brodie, 2004); intermediate values of n have been suggested to be related to grain boundary sliding (e.g., Goldsby & Kohlstedt, 2001; Hansen et al., 2011), although it is important to note that this mechanism is intrinsically coupled to either diffusion or dislocation creep (Hansen et al., 2011; Raj & Ashby, 1971). In addition to mechanical processes, thermal effects can also be relevant to lithospheric deformation. Thermal effects are typically thought of in terms of the steady-state geothermal gradient, but this thermal profile can be perturbed by viscous heating during rapid shear and an associated thermal diffusion (Moore & Parsons, 2015; Takeuchi & Fialko, 2013). As a consequence, the effective power law i inferred at the kilometer scale need not be bounded between 1 and 4, but instead may be even higher (e.g., Kelemen & Hirth, 2007).

If any of the individual parameters in Equation 12 evolve with incremental strain or time, for example, temperature or grain size (Allison & Dunham, 2021; Montési & Hirth, 2003), then there would not be a unique relationship between $\dot{\varepsilon}$ and σ until a steady state is reached. The viscous creep that would result from this equilibration process is often called "transient creep," and is an important motivation for invoking Burgers rheology (Chopra, 1997; Freed et al., 2012; Post, 1977). Despite the likely presence of viscous transients, we maintain that the principle of parsimony dictates that we choose steady-state power-law rheologies over Burgers rheologies for modeling geodetic data. To further illustrate this preference, we draw parallels between the aforementioned transient viscous creep and deviations from steady-state frictional strength in rock friction experiments. Unsteady evolution of the friction coefficient is captured by a state variable, θ, which is thought to represent the quality and/or average timescale of asperity contact during frictional sliding (Marone, 1998; Scholz, 1998). Despite the well-known importance of θ to many aspects of frictional mechanics (Scholz, 2002), geodetic investigations of frictional afterslip are rarely able to resolve the evolution of the frictional state from the data. Even when the state evolution is identified, it is shown to quickly evolve toward steady state within a few hours and may be invisible to typical (sampled daily) postseismic time series (Fukuda et al., 2009; Perfettini & Ampuero, 2008). This argument does not obviate the existence or importance of unsteady strength evolution, but instead emphasizes that it is not necessary to invoke an unsteady Burgers rheology when steady-state power-law rheologies can explain the available geodetic observations. As a result, we are tempted to interpret the value of $\hat{n} \geq 3$ in terms of a rheology dominated by dislocation creep, with possible contributions from thermomechanically coupled processes such as shear heating and grain boundary sliding.

4.2.2. Averaging Over Spatially Variable Parameters

The inferred $\hat{A}, i$ values do not only represent averages over multiple physical and chemical processes, but also over a spatially varying set of parameters. The dominant contribution of this in Equation 12 likely comes from the depth-dependence of temperature, that is, $T(x_3) \propto x_3$. However, our ability to geodetically infer spatially varying rheological parameters is limited by the spatial smearing effect of elasticity as well as the apparent homogenization of rheological properties during shear (e.g., Almeida et al., 2018; Hetland & Hager, 2006; Ray & Viesca, 2019). This implies that we may at best infer a best-fitting $\hat{A}, i$ from a single earthquake cycle, with larger events eliciting a response from greater depths and hence a larger $\hat{A} \propto \exp\left(\frac{-Q}{RT}\right)$. The way forward then is to use sequences of earthquakes (events of different magnitudes and/or depth on the same fault), where each individual earthquake may be mapped to a set of uniform $\hat{A}, i$ but these parameters show a consistent pattern, such as a fixed i but $\hat{A}$ increases with increasing size or depth of the earthquake. The implication then is that spatial heterogeneity is necessary to explain the observations and therefore we can infer more about how the lithosphere behaves.

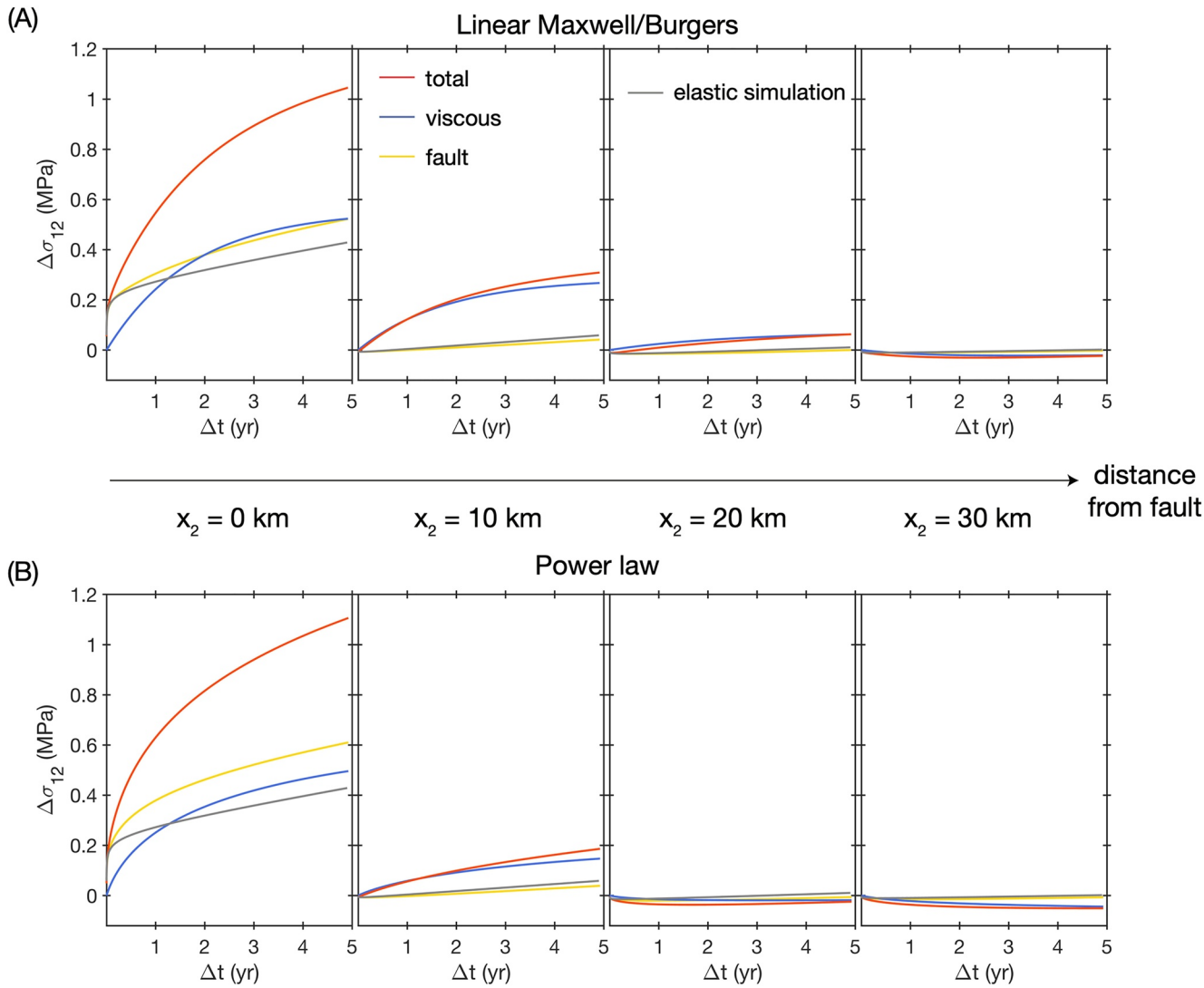

Figure 9. Stress change and decomposition into contributions from fault slip and viscous shear for (a) linear Burgers rheology ($\eta_k = 3 \times 10^{18}$, $\eta_M = 10^{20}$ Pa-s) with effective viscosity $\sim 5 \times 10^{18}$ Pa-s in the plotted time window, and (b) power law rheology with $n = 3$, $A^{-1} = 10^{19}$. Stress is plotted at 0, 10, 20, and 30 km away from the fault at 10 km depth. Total stress evolution from a nearly elastic model (linear Maxwell simulation with $\eta_M = 10^{20}$ Pa-s) is also shown (gray). The stress evolution over the first 5 years is dominated by the viscoelastic response for linear and power-law rheologies. Additionally, due to the mechanical coupling between fault slip and viscous shear, stress transfer from fault slip evolution in the viscoelastic simulations is significantly different from the elastic simulations.

4.3. Coupling Between Frictional Slip and Viscous Creep

An important implication of mechanically coupled models of fault slip and distributed deformation, such as our simulations, is that stress-driven interactions between frictional afterslip on the fault and distributed viscous flow in the lower crust and mantle are not independent processes, as is typically considered in many inverse postseismic modeling studies. This simplification explicitly decouples the mechanical interactions between frictional afterslip and viscous creep, and has been shown to systematically bias the location and amplitude of inferred slip and strain (e.g., Muto et al., 2019; Peña et al., 2020). Our simulation results suggest that a permissible simplification may be to treat earthquake-driven viscoelastic relaxation as an independent process, while afterslip is driven by the coseismic stress change as well as the subsequent viscous flow of the bulk medium (Figure A2). We highlight this by noting the amplitude and temporal evolution of afterslip is markedly different between simulations that consider a purely elastic medium versus a viscoelastic medium (Figure 9).

4.3.1. Time-Dependent Loading Rate

The effect of viscoelastic relaxation on afterslip can be thought of as a modification of the stress loading rate along the fault. For an isolated system, the governing equation for frictional slip in response to a coseismic stress step is $k\,(v^{\infty} - v(t)) \propto \frac{\mathrm{d}f(v(t))}{\mathrm{d}t}$ where f is the velocity dependent friction coefficient, k is the elastic stiffness, and v^{∞} is the long-term slip rate of the fault (Marone et al., 1991). When viscoelastic relaxation of the medium is factored in, the loading term now contains two contributions—a time-invariant contribution from v^{∞}, and time-dependent stress transfer due to viscous creep in the surrounding medium (Pollitz, 2017, 2012). Viscous creep is itself a decaying function in time, with the exact decay rate being a function of the rheology (Figure 3). Thus, the effective loading rate for afterslip is no longer time-invariant (Figure A2) and the resulting time series for slip and stress transferred to the surrounding medium can notably differ from simulations that decouple afterslip and viscous creep (Figure 9).

4.3.2. Regional Stress Interactions

The difference in time-dependent loading between purely elastic fault models and those considering viscoelastic deformation suggests that viscoelastic interactions are an important ingredient for efforts aimed at modeling regional tectonics and multifault interactions, particularly given that the spatial footprint of this distributed deformation can be much larger than that of slip on individual faults (Figures 3 and 4). Viscoelastic stress interactions have been noted to be relevant to along-strike stress transfer and timing of a recent sequence of great earthquakes on the North Anatolian Fault (Devries & Meade, 2016; Devries et al., 2017), and Southern California (e.g., Freed & Lin, 2001). More generally, time-dependent loading alters the stress state on the fault preceding dynamic rupture. This pre-rupture stress state has been noted to control many aspects of the rupture process from earthquake nucleation to rupture arrest, including the likelihood of ruptures propagating over multiple fault segments (e.g., Lambert et al., 2021; Lambert & Lapusta, 2021; Noda et al., 2009; Ulrich et al., 2019; Zheng & Rice, 1998).

Time-dependent loading due to viscous creep may be particularly important when considering interactions between major plate boundary faults and neighboring lower slip rate faults (Freed, 2005; Kenner & Simons, 2005). For low slip rate faults, the loading due to the long-term tectonic loading rate, which is relatively small for low v^{∞}, may be overwhelmed by the static stress transfer from a nearby earthquake and the corresponding viscous response of the ductile lower crust and mantle (Figure 9). As a result, seismicity on such low slip rate faults may cluster in time with large earthquakes on the major plate boundary fault and may be indicative of coordinated time-dependent loading, as opposed to an individual long-term loading rate of each fault within this system. Future work is needed to develop more realistic treatments of fault loading in larger-scale simulations of fault networks and models of seismic hazard (e.g., Shaw et al., 2018; Tullis et al., 2012), potentially including physically motivated approximations of viscoelastic contributions to the effective loading rate of fault populations.

5. Conclusions

Geodetic recordings of earthquake cycle deformation related to large earthquakes provide geoscientists with one of the best opportunities to estimate the effective rheology of the lithosphere-asthenosphere system. In this article, we showed that combining geodetic observations with numerical simulations of the earthquake cycle translate into better estimates of rheological models and relevant parameters. Below we list a number of important contributions and insight from this study.

1. We developed a numerical framework to model the earthquake cycle, including interactions between frictional sliding on faults and viscous deformation of the upper mantle, that is computationally inexpensive (can be run on personal computers). This facilitates efficient exploration of various rheological models and parameters.
2. By incorporating geodetic observations throughout the entire earthquake cycle, the ambiguity associated with commonly used rheological models is reduced. Specifically, a homogeneous linear Maxwell viscoelastic medium is simply inconsistent with typical geodetic observations.
3. The average viscoelastic description of the lithosphere may be that of a power-law spring-dashpot system, although Burgers rheologies may also satisfactorily explain the data but invoke more tunable parameters.
4. Our preferred parameterization of the viscous element in this spring-dashpot system follows a steady-state flow low of the form $\dot{\varepsilon} = A\sigma^{n}$, and the parameter ranges for the pre-factor $1/A$ range from 10^{18} to 10^{20} and the power exponent $n \geq 3$. The power exponent $n \geq 3$ may strongly hint at dislocation creep being a dominant process throughout the earthquake cycle. However, we caution direct interpretation of these parameters from single earthquake relaxation studies.

5. Differentiating between these rheologies requires geodetic observations from earthquake sequences (events of different magnitudes). The postseismic response of power-law rheologies will show strong magnitude-dependence while the linear Burgers body will not.
6. An important societal consequence of lithospheric viscoelasticity is to modify the spatial and temporal pattern of stress interactions between faults and the surrounding bulk, compared to purely elastic models. This leads to significantly stronger temporal linkage and long-distance interactions, and hence seismicity, between faults than expected by frictional-elastic models of faults.

Appendix

A1. Equivalence Between Afterslip and Viscous Creep

To demonstrate the equivalence between rate-strengthening frictional sliding and a power-law viscous creep, we consider a common strain rate variable v. The governing ODE for a steady-state elasto-frictional system is given by,

$$k\,(v - v^{\infty}) = (a - b)\sigma_n \frac{\dot{v}}{v} \tag{A1}$$

while for a power-law viscoelastic system, the governing ODE is

$$k\,(v - v^{\infty}) = \frac{1}{n}\left(\frac{v}{A}\right)^{\frac{1}{n}} \frac{\dot{v}}{v}. \tag{A2}$$

It is clear that the equivalence between the two systems occurs as $\left(\frac{v}{A}\right)^{\frac{1}{n}}$ (this is actually the stress level in the system) approaches a constant value over the domain of v, at least in comparison to $k\,(v - v^{\infty})$. When $n = 6$, the

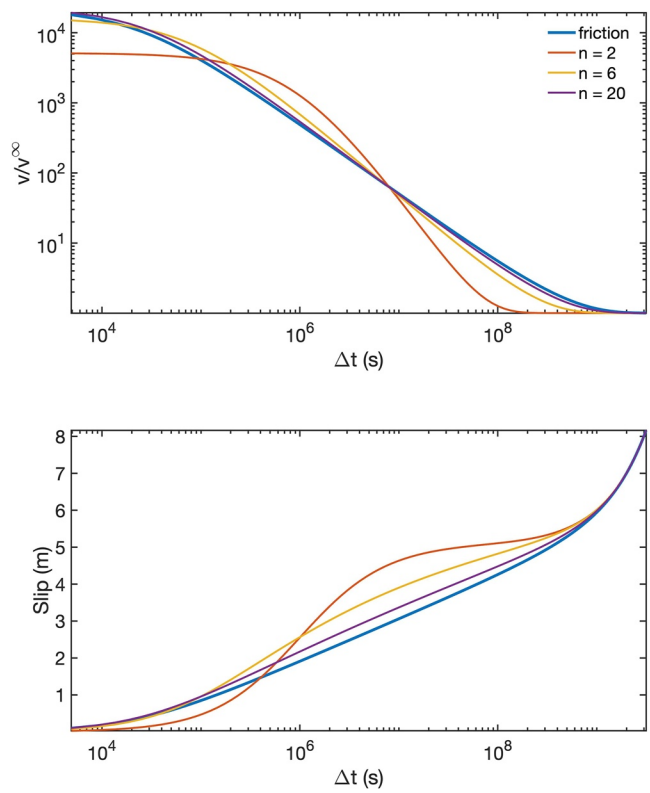

Figure A1. Approximation of frictional slip with a power-law in a simplified spring-dashpot analysis. As power-law exponent n increases, the error in the approximation reduces. The top panel shows velocity evolution for three different values of n while the bottom panel shows slip evolution.

viscous strain rate changes by ~3 orders of magnitude in some of our simulations. The resulting $\left(\frac{v}{A}\right)^{\frac{1}{n}}$ varies by ~3 over the duration of the entire earthquake cycle. The variation by a factor of 3 also occurs slowly in time which means that for typical geodetic observational windows, $n = 6$ is sufficiently close to an equivalent logarithmic system and vice-versa (Figure A1).

A2. Relative Contributions of Afterslip and Viscous Creep in a Coupled System

In an elasto-visco-frictional system that explicitly demarcates the nonelastic domain into frictional and viscous regimes as shown in Figure A2, we show that the mechanical coupling between afterslip and viscous creep may be reduced to a one-way coupling problem such that afterslip is driven by a time-invariant background loading as well as time-dependent stress transfer from the viscous domain; the viscous strain rates on the other hand appear to evolve nearly independently of afterslip (Figure A2).

The time evolution of the slip rate on a velocity-strengthening frictional fault is given as a function of the initial condition $v(0)$ and a relaxation timescale t_R,

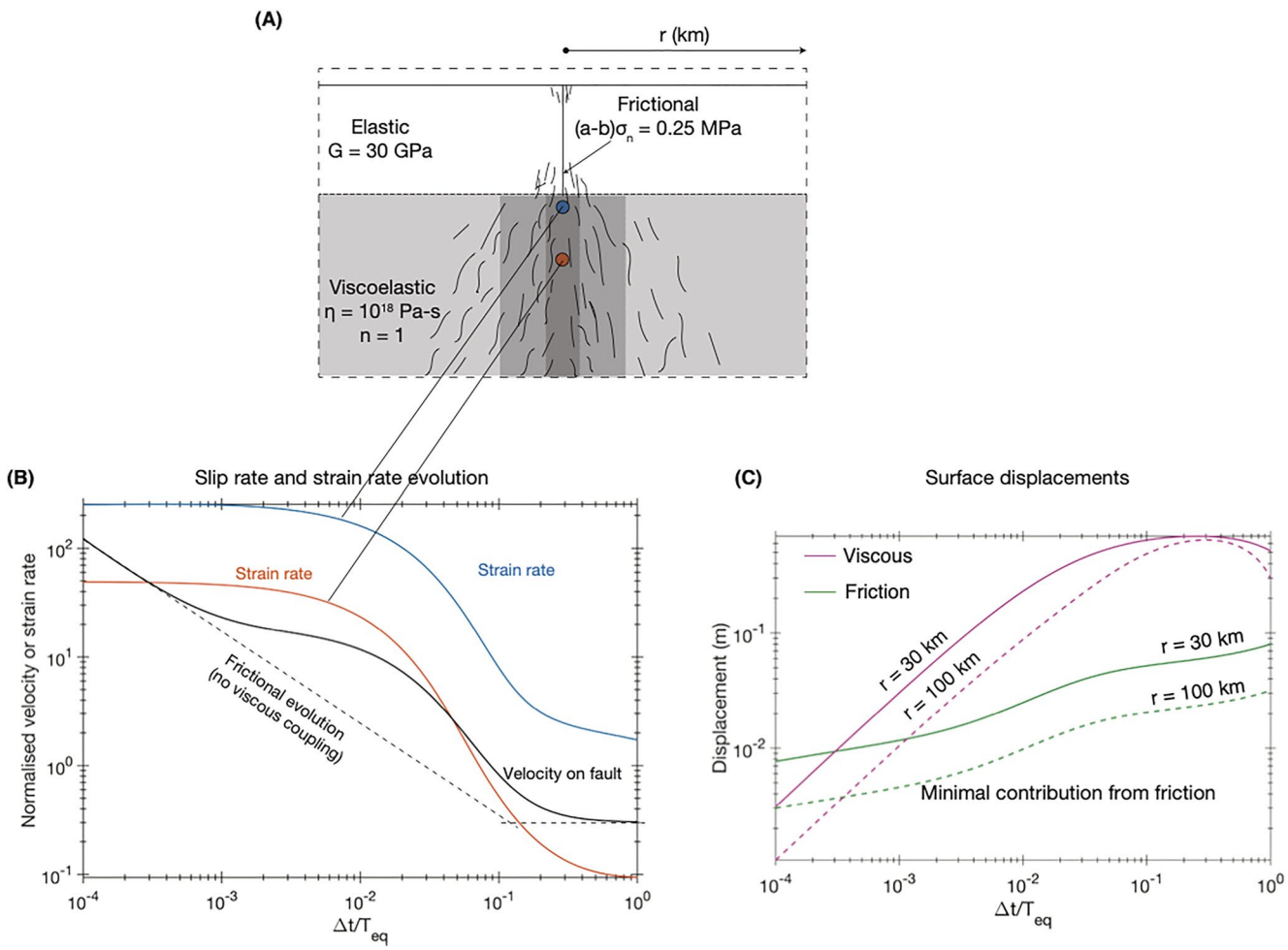

Figure A2. (a) Numerical modeling setup and parameters used for a mechanically coupled visco-elasto-frictional system. (b) Viscous strain rate and on-fault velocity evolution shows the influence of viscous deformation on frictional velocity evolution. Dashed lines show theoretical frictional creep in an isolated elasto-frictional system. (c) Surface displacement time series due to viscous (magenta) and frictional creep (green) arising from lower crustal and upper mantle deformation (shallow creep is not considered here). Left panel shows displacement evolution at $r = 30$, 100 km (continuous line—30 km, dashed line—100 km). Right panel shows the percentage contribution of viscous creep to the surface displacement time series as a function of time and space.

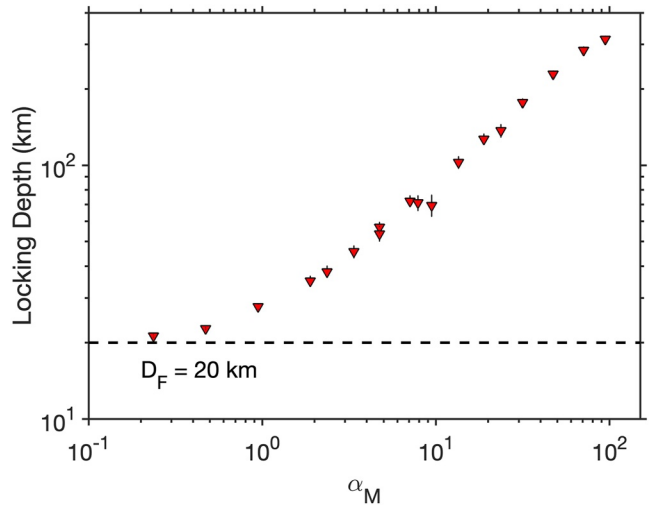

Figure A3. Variation of the geodetically estimated late interseismic locking depth for a linear Maxwell rheology as a function of the rheological parameter α_M. $\alpha_M = \frac{GT_{eq}}{2\eta_M}$ is a dimensionless parameter that combines rheological properties and the recurrence time of the earthquake cycle. Small α_M corresponds to a nearly elastic material, and hence minimal earthquake cycle effects while large α_M corresponds to a low viscosity material and pronounced earthquake cycle effects.

$$v(t) = \frac{v(0)}{\frac{v(0)}{v^{\infty}} + e^{\frac{-t}{t_R}}\left(1 - \frac{v(0)}{v^{\infty}}\right)} \tag{A3}$$

The relaxation timescale here corresponds to a different model than the one discussed in Figure 6. However, considering the parameters we used in our suite of simulations (Table 1), the equivalent relaxation timescale for the frictional fault is significantly smaller than the relaxation times for at least the linear Maxwell systems.

This decaying signal appears as a straight line on a logarithmic scale, and then will smoothly transition to the background loading velocity (Figure A2—dashed lines). However, in the presence of viscous deformation in the mantle, frictional slip mimics the time evolution of viscous creep beyond an initial logarithmic decay (Figure A2). The resulting displacement time series at the free surface reflects this behavior, and shows that beyond an initial logarithmic growth of displacements due to frictional slip, this physical process is entirely masked by the surface contributions of viscous creep (Figure A2).

Data Availability Statement

No data was used in this study. All the MATLAB code required to recreate the results of this study is available at the Caltech data repository https://data.caltech.edu/records/20257 (DOI: 10.22002/D1.20257).

Acknowledgments
This research was supported by a Texaco Postdoctoral Fellowship awarded to Rishav Mallick. Valere Lambert is supported by a National Science Foundation EAR Postdoctoral Fellowship. The authors thank JGR editor Paul Tregoning, associate editor Mike Poland, Hugo Perfettini and an anonymous reviewer for their review and feedback on this manuscript. The authors are grateful to Roland Bürgmann and Judith Hubbard for discussions and suggestions for this project.

References

Allison, K. L., & Dunham, E. M. (2017). Earthquake cycle simulations with rate-and-state friction and power-law viscoelasticity. *Tectonophysics*, *733*, 232–256. https://doi.org/10.1016/j.tecto.2017.10.021

Allison, K. L., & Dunham, E. M. (2021). Influence of shear heating and thermomechanical coupling on earthquake sequences and the brittle-ductile transition. *Journal of Geophysical Research: Solid Earth*, *126*(6), 1–28. https://doi.org/10.1029/2020jb021394

Almeida, R., Lindsey, E. O., Bradley, K., Hubbard, J., Mallick, R., & Hill, E. M. (2018). Can the updip limit of frictional locking on megathrusts be detected geodetically? Quantifying the effect of stress shadows on near-trench coupling. *Geophysical Research Letters*, *45*, 4754–4763. https://doi.org/10.1029/2018GL077785

Barbot, S. (2018). Deformation of a half-space from anelastic strain confined in a tetrahedral volume. *Bulletin of the Seismological Society of America*, *108*(5A), 2687–2712. https://doi.org/10.1785/0120180058

Bruhat, L., Barbot, S., & Avouac, J. P. (2011). Evidence for postseismic deformation of the lower crust following the 2004 Mw6.0 Parkfield earthquake. *Journal of Geophysical Research: Solid Earth*, *116*(8), 1–10. https://doi.org/10.1029/2010JB008073

Bürgmann, R. (2018).The geophysics, geology and mechanics of slow fault slip. *Earth and Planetary Science Letters*, *495*, 112–134. https://doi.org/10.1016/j.epsl.2018.04.062

Bürgmann, R., & Dresen, G. (2008). Rheology of the lower crust and upper mantle: Evidence from rock mechanics, geodesy, and field observations. *Annual Review of Earth and Planetary Sciences*, *36*(1), 531–567. https://doi.org/10.1146/annurev.earth.36.031207.124326

Chopra, P. N. (1997). High-temperature transient creep in olivine rocks. *Tectonophysics*, *279*(1–4), 93–111. https://doi.org/10.1016/s0040-1951(97)00134-0

Chopra, P. N., & Paterson, M. S. (1981). The experimental deformation of dunite. *Tectonophysics*, *78*(1–4), 453–473. https://doi.org/10.1016/0040-1951(81)90024-X

Cohen, S. C., & Kramer, M. J. (1984). Crustal deformation, the earthquake cycle, and models of viscoelastic flow in the asthenosphere. *Geophysical Journal International*, *78*(3), 735–750. https://doi.org/10.1111/j.1365-246X.1984.tb05068.x

Devries, P. M., Krastev, P. G., Dolan, J. F., & Meade, B. J. (2017). Viscoelastic block models of the North Anatolian Fault: A unified earthquake cycle representation of pre- and postseismic geodetic observations. *Bulletin of the Seismological Society of America*, *107*(1), 403–417. https://doi.org/10.1785/0120160059

Devries, P. M., & Meade, B. J. (2013). Earthquake cycle deformation in the Tibetan plateau with a weak mid-crustal layer. *Journal of Geophysical Research: Solid Earth*, *118*(6), 3101–3111. https://doi.org/10.1002/jgrb.50209

Devries, P. M., & Meade, B. J. (2016). Kinematically consistent models of viscoelastic stress evolution. *Geophysical Research Letters*, *43*(9), 4205–4214. https://doi.org/10.1002/2016GL068375

Duputel, Z., Agram, P. S., Simons, M., Minson, S. E., & Beck, J. L. (2014). Accounting for prediction uncertainty when inferring subsurface fault slip. *Geophysical Journal International*, *197*(1), 464–482. https://doi.org/10.1093/gji/ggt517

England, P. C., Walker, R. T., Fu, B., & Floyd, M. A. (2013). A bound on the viscosity of the Tibetan crust from the horizontality of palaeolake shorelines. *Earth and Planetary Science Letters*, *375*, 44–56. https://doi.org/10.1016/j.epsl.2013.05.001

Freed, A. M. (2005). Earthquake triggering by static, dynamic, and postseismic stress transfer. *Annual Review of Earth and Planetary Sciences*, *33*(1), 335–367. https://doi.org/10.1146/annurev.earth.33.092203.122505

Freed, A. M., & Bürgmann, R. (2004). Evidence of power-law flow in the Mojave Desert mantle. *Nature*, *430*(6999), 548–551. https://doi.org/10.1038/nature02784

Freed, A. M., Herring, T., & Bürgmann, R. (2010). Steady-state laboratory flow laws alone fail to explain postseismic observations. *Earth and Planetary Science Letters*, *300*(1–2), 1–10. https://doi.org/10.1016/j.epsl.2010.10.005

Freed, A. M., Hirth, G., & Behn, M. D. (2012). Using short-term postseismic displacements to infer the ambient deformation conditions of the upper mantle. *Journal of Geophysical Research: Solid Earth*, *117*(B1). https://doi.org/10.1029/2011JB008562

Freed, A. M., & Lin, J. (2001). Delayed triggering of the 1999 Hector Mine earthquake by viscoelastic stress transfer. *Nature*, *411*(6834), 180–183. https://doi.org/10.1038/35075548

Freymueller, J. T., Cohen, S. C., & Fletcher, H. J. (2000). Spatial variations in present-day deformation, Kenai Peninsula, Alaska, and their implications. *Journal of Geophysical Research: Solid Earth*, *105*(B4), 8079–8101. https://doi.org/10.1029/1999jb900388

Fukuda, J., Johnson, K. M., Larson, K. M., & Miyazaki, S. (2009). Fault friction parameters inferred from the early stages of afterslip following the 2003 Tokachi-oki earthquake. *Journal of Geophysical Research*, *114*(B4). https://doi.org/10.1029/2008JB006166

Goldsby, D. L., & Kohlstedt, D. L. (2001). Superplastic deformation of ice: Experimental observations. *Journal of Geophysical Research: Solid Earth*, *106*(B6), 11017–11030. https://doi.org/10.1029/2000jb900336

Hansen, L. N., Zimmerman, M. E., & Kohlstedt, D. L. (2011). Grain boundary sliding in San Carlos olivine: Flow law parameters and crystallographic-preferred orientation. *Journal of Geophysical Research: Solid Earth*, *116*(8), 1–16. https://doi.org/10.1029/2011JB008220

Hearn, E. H., & Thatcher, W. R. (2015). Reconciling viscoelastic models of postseismic and interseismic deformation: Effects of viscous shear zones and finite length ruptures. *Journal of Geophysical Research: Solid Earth*, *120*(4), 2794–2819. https://doi.org/10.1002/2014JB011361

Henriquet, M., Avouac, J. P., & Bills, B. G. (2019). Crustal rheology of southern Tibet constrained from lake-induced viscoelastic deformation. *Earth and Planetary Science Letters*, *506*, 308–322. https://doi.org/10.1016/j.epsl.2018.11.014

Hetland, E. A., & Hager, B. H. (2005). Postseismic and interseismic displacements near a strike-slip fault: A two-dimensional theory for general linear viscoelastic rheologies. *Journal of Geophysical Research: Solid Earth*, *110*(10), 1–21. https://doi.org/10.1029/2005JB003689

Hetland, E. A., & Hager, B. H. (2006). The effects of rheological layering on post-seismic deformation. *Geophysical Journal International*, *166*(1), 277–292. https://doi.org/10.1111/j.1365-246X.2006.02974.x

Hirth, G. (2002). Laboratory constraints on the rheology of the upper mantle. *Reviews in Mineralogy and Geochemistry*, *51*, 97–120. https://doi.org/10.2138/gsrmg.51.1.97

Hirth, G., & Kohlstedt, D. L. (2003). Rheology of the upper mantle and the mantle wedge: A view from the experimentalists. *Geophysical Monograph Series*, *138*, 83–105. https://doi.org/10.1029/138gm06

Hussain, E., Wright, T. J., Walters, R. J., Bekaert, D. P., Lloyd, R., & Hooper, A. (2018). Constant strain accumulation rate between major earthquakes on the North Anatolian Fault. *Nature Communications*, *9*(1), 1–9. https://doi.org/10.1038/s41467-018-03739-2

Johnson, K. M., & Segall, P. (2004). Viscoelastic earthquake cycle models with deep stress-driven creep along the San Andreas fault system. *Journal of Geophysical Research B: Solid Earth*, *109*(10), 1–19. https://doi.org/10.1029/2004JB003096

Jónsson, S., Segall, P., Pedersen, R., & Björnsson, G. (2003). Post-earthquake ground movements correlated to pore-pressure transients. *Nature*, *424*(6945), 179–183. https://doi.org/10.1038/nature01776

Kanamori, H., & Brodsky, E. E. (2004). The physics of earthquakes. *Reports on Progress in Physics*, *67*(8), 1429–1496. https://doi.org/10.1088/0034-4885/67/8/R03

Karato, S.-I., Paterson, M., & Fitzgerald, D. (1986). Rheology of synthetic olivine aggregates: Influence of grain size and water. *Journal of Geophysical Research*, *91*(B8), 8151–8176. https://doi.org/10.1029/jb091ib08p08151

Kaufmann, G., & Amelung, F. (2000). Reservoir-induced deformation and continental rheology in vicinity of Lake Mead, Nevada. *Journal of Geophysical Research: Solid Earth*, *105*(B7), 16341–16358. https://doi.org/10.1029/2000JB900079

Kelemen, P. B., & Hirth, G. (2007). A periodic shear-heating mechanism for intermediate-depth earthquakes in the mantle. *Nature*, *446*(7137), 787–790. https://doi.org/10.1038/nature05717

Kenner, S. J., & Segall, P. (2003). Lower crustal structure in northern California: Implications from strain rate variations following the 1906 San Francisco earthquake. *Journal of Geophysical Research: Solid Earth*, *108*(B1). https://doi.org/10.1029/2001jb000189

Kenner, S. J., & Simons, M. (2005). Temporal clustering of major earthquakes along individual faults due to post-seismic reloading. *Geophysical Journal International*, *160*(1), 179–194. https://doi.org/10.1111/j.1365-246X.2005.02460.x

Khazaradze, G., Wang, K., Klotz, J., Hu, Y., & He, J. (2002). Prolonged post-seismic deformation of the 1960 great Chile earthquake and implications for mantle rheology. *Geophysical Research Letters*, *29*(22). https://doi.org/10.1029/2002gl015986

Khoshmanesh, M., & Shirzaei, M. (2018). Episodic creep events on the San Andreas Fault caused by pore pressure variations. *Nature Geoscience*, *11*(8), 610–614. https://doi.org/10.1038/s41561-018-0160-2

Lambert, V., & Barbot, S. (2016). Contribution of viscoelastic flow in earthquake cycles within the lithosphere-asthenosphere system. *Geophysical Research Letters*, *43*(19), 10142–10154. https://doi.org/10.1002/2016GL070345

Lambert, V., & Lapusta, N. (2021). Resolving simulated sequences of earthquakes and fault interactions: Implications for physics-based seismic hazard assessment. *Journal of Geophysical Research: Solid Earth*, *126*(10), e2021JB022193. https://doi.org/10.1029/2021JB022193

Lambert, V., Lapusta, N., & Faulkner, D. (2021). Scale dependence of earthquake rupture prestress in models with enhanced weakening: Implications for event statistics and inferences of fault stress. *Journal of Geophysical Research: Solid Earth*, *126*(10), 1–29. https://doi.org/10.1029/2021JB021886

Larsen, C. F., Motyka, R. J., Freymueller, J. T., Echelmeyer, K. A., & Ivins, E. R. (2005). Rapid viscoelastic uplift in southeast Alaska caused by post-Little Ice Age glacial retreat. *Earth and Planetary Science Letters*, *237*(3–4), 548–560. https://doi.org/10.1016/j.epsl.2005.06.032

Lehner, F. K., & Li, V. C. (1982). Large-scale characteristics of plate boundary deformations related to the post-seismic readjustment of a thin asthenosphere. *Geophysical Journal International*, *71*(3), 775–792. https://doi.org/10.1111/j.1365-246X.1982.tb02797.x

Li, V. C., & Rice, J. R. (1987). Crustal deformation in Great California earthquake cycles. *Journal of Geophysical Research*, *92*(B11), 11533–11551. https://doi.org/10.1029/JB092iB11p11533

Lyzenga, G. A., Raefsky, A., & Mulligan, S. G. (1991). Models of recurrent strike-slip earthquake cycles and the state of crustal stress. *Journal of Geophysical Research: Solid Earth*, *96*(B13), 21623–21640. https://doi.org/10.1029/91JB02260

Mallick, R., Bürgmann, R., Johnson, K., & Hubbard, J. (2021). A unified framework for earthquake sequences and the growth of geological structure in fold-thrust belts. *Journal of Geophysical Research: Solid Earth*, *126*(9), 1–26. https://doi.org/10.1029/2021JB022045

Mallick, R., Meltzner, A. J., Tsang, L. L. H., Lindsey, E. O., Feng, L., & Hill, E. M. (2021). Long-lived shallow slow-slip events on the Sunda megathrust. *Nature Geoscience*, *14*(5), 327–333. https://doi.org/10.1038/s41561-021-00727-y

Marone, C. (1998). Laboratory-derived friction laws and their application to seismic faulting. *Annual Review of Earth and Planetary Sciences*, *26*(1), 643–696. https://doi.org/10.1146/annurev.earth.26.1.643

Marone, C., Scholz, C. H., & Bilham, R. (1991). On the mechanics of earthquake afterslip. *Journal of Geophysical Research*, *96*(B5), 8441–8452. https://doi.org/10.1029/91jb00275

Melnick, D., Li, S., Moreno, M., Cisternas, M., Jara-Muñoz, J., Wesson, R., et al. (2018). Back to full interseismic plate locking decades after the giant 1960 Chile earthquake. *Nature Communications*, *9*(1), 3527. https://doi.org/10.1038/s41467-018-05989-6

Milne, G. A., Davis, J. L., Mitrovica, J. X., Scherneck, H. G., Johansson, J. M., Vermeer, M., & Koivula, H. (2001). Space-geodetic constraints on glacial isostatic adjustment in fennoscandia. *Science*, *291*(5512), 2381–2385. https://doi.org/10.1126/science.1057022

Minson, S. E., Simons, M., & Beck, J. L. (2013). Bayesian inversion for finite fault earthquake source models I-theory and algorithm. *Geophysical Journal International*, *194*(3), 1701–1726. https://doi.org/10.1093/gji/ggt180

Montési, L. G. (2004). Controls of shear zone rheology and tectonic loading on postseismic creep. *Journal of Geophysical Research: Solid Earth*, *109*(10). https://doi.org/10.1029/2003JB002925

Montési, L. G., & Hirth, G. (2003). Grain size evolution and the rheology of ductile shear zones: From laboratory experiments to postseismic creep. *Earth and Planetary Science Letters*, *211*(1–2), 97–110. https://doi.org/10.1016/S0012-821X(03)00196-1

Moore, J. D., & Parsons, B. (2015). Scaling of viscous shear zones with depth-dependent viscosity and power-law stress-strain-rate dependence. *Geophysical Journal International*, *202*(1), 242–260. https://doi.org/10.1093/gji/ggv143

Moore, J. D. P., Yu, H., Tang, C.-H., Wang, T., Barbot, S., Peng, D., et al. (2017). Imaging the distribution of transient viscosity after the 2016 M w 7.1 Kumamoto earthquake. *Science*, *356*(6334), 163–167. https://doi.org/10.1126/science.aal3422

Müller, G. (1986). Generalized Maxwell bodies and estimates of mantle viscosity. *Geophysical Journal of the Royal Astronomical Society*, *87*(3), 1113–1141. https://doi.org/10.1111/j.1365-246X.1986.tb01986.x

Mulyukova, E., & Bercovici, D. (2019). The generation of plate tectonics from grains to global scales: A brief review. *Tectonics*, *38*(12), 4058–4076. https://doi.org/10.1029/2018TC005447

Muto, J., Moore, J. D. P., Barbot, S., Iinuma, T., Ohta, Y., & Iwamori, H. (2019). Coupled afterslip and transient mantle flow after the 2011 Tohoku earthquake. *Science Advances*, *5*(9), eaaw1164. https://doi.org/10.1126/sciadv.aaw1164

Noda, H., Dunham, E. M., & Rice, J. R. (2009). Earthquake ruptures with thermal weakening and the operation of major faults at low overall stress levels. *Journal of Geophysical Research: Solid Earth*, *114*(7), 1–27. https://doi.org/10.1029/2008JB006143

NSF. (2020), *A Vision for NSF Earth Sciences 2020-2030*, National Academies Press. https://doi.org/10.17226/25761

Peña, C., Heidbach, O., Moreno, M., Bedford, J., Ziegler, M., Tassara, A., & Oncken, O. (2020). Impact of power-law rheology on the viscoelastic relaxation pattern and afterslip distribution following the 2010 Mw 8.8 Maule earthquake. *Earth and Planetary Science Letters*, *542*, 116292. https://doi.org/10.1016/j.epsl.2020.116292

Peltzer, G., Rosen, P., Rogez, F., & Hudnut, K. (1998). Poroelastic rebound along the Landers 1992 earthquake surface rupture. *Journal of Geophysical Research: Solid Earth*, *103*(B12), 30131–30145. https://doi.org/10.1029/98jb02302

Perfettini, H., & Ampuero, J.-P. P. (2008). Dynamics of a velocity strengthening fault region: Implications for slow earthquakes and postseismic slip. *Journal of Geophysical Research*, *113*(B9). https://doi.org/10.1029/2007JB005398

Perfettini, H., & Avouac, J.-P. (2004). Stress transfer and strain rate variations during the seismic cycle. *Journal of Geophysical Research: Solid Earth*, *109*(B6), 1–8. https://doi.org/10.1029/2003JB002917

Pollitz, F. F. (2005). Transient rheology of the upper mantle beneath central Alaska inferred from the crustal velocity field following the 2002 Denali earthquake. *Journal of Geophysical Research: Solid Earth*, *110*(8), 1–16. https://doi.org/10.1029/2005JB003672

Pollitz, F. F. (2012). ViscoSim earthquake simulator. *Seismological Research Letters*, *83*(6), 979–982. https://doi.org/10.1785/0220120050

Pollitz, F. F. (2017). A note on adding viscoelasticity to earthquake simulators. *Bulletin of the Seismological Society of America*, *107*(1), 468–474. https://doi.org/10.1785/0120160192

Pollitz, F. F. (2019). Lithosphere and shallow asthenosphere rheology from observations of post-earthquake relaxation. *Physics of the Earth and Planetary Interiors*, *293*, 106271. https://doi.org/10.1016/j.pepi.2019.106271

Post, R. L. (1977). High-temperature creep of Mt. Burnet Dunite. *Tectonophysics*, *42*(2–4), 75–110. https://doi.org/10.1016/0040-1951(77)90162-7

Raj, R., & Ashby, M. F. (1971). On grain boundary sliding and diffusional creep. *Metallurgical Transactions A*, *2*(4), 1113–1127. https://doi.org/10.1007/BF02664244

Ray, S., & Viesca, R. C. (2019). Homogenization of fault frictional properties. *Geophysical Journal International*, *219*(2), 1203–1211. https://doi.org/10.1093/gji/ggz327

Reches, Z., Schubert, G., & Anderson, C. (1994). Modeling of periodic great earthquakes on the San Andreas fault: Effects of nonlinear crustal rheology. *Journal of Geophysical Research*, *99*(B11), 983–1000. https://doi.org/10.1029/94jb00334

Rutter, E., & Brodie, K. (2004). Experimental grain size-sensitive flow of hot-pressed Brazilian quartz aggregates. *Journal of Structural Geology*, *26*(11), 2011–2023. https://doi.org/10.1016/j.jsg.2004.04.006

Ryder, I., Parsons, B., Wright, T. J., & Funning, G. J. (2007). Post-seismic motion following the 1997 Manyi (Tibet) earthquake: InSAR observations and modelling. *Geophysical Journal International*, *169*(3), 1009–1027. https://doi.org/10.1111/j.1365-246X.2006.03312.x

Savage, J., & Svarc, J. (2009). Postseismic relaxation following the 1992 m7. 3 landers and 1999 m7. 1 hector mine earthquakes, southern California. *Journal of Geophysical Research: Solid Earth*, *114*(B1). https://doi.org/10.1029/2008jb005938

Savage, J. C. (2000). Viscoelastic-coupling model for the earthquake cycle driven from below. *Journal of Geophysical Research*, *105*(B11), 25525–25532. https://doi.org/10.1029/2000JB900276

Savage, J. C., & Burford, R. O. (1973). Geodetic determination of relative plate motion in central California. *Journal of Geophysical Research*, *78*(5), 832–845. https://doi.org/10.1029/jb078i005p00832

Savage, J. C., & Prescott, W. H. (1978). Asthenosphere readjustment and the earthquake cycle. *Journal of Geophysical Research: Solid Earth*, *83*(B7), 3369–3376. https://doi.org/10.1029/jb083ib07p03369

Savage, J. C., Svarc, J. L., Prescott, W., & Hudnut, K. W. (1998). Deformation following the 1994 northridge earthquake (m= 6.7), southern California. *Geophysical Research Letters*, *25*(14), 2725–2728. https://doi.org/10.1029/98gl02058

Scholz, C. H. (1998). Earthquakes and friction laws. *Nature*, *391*, 37–42. https://doi.org/10.1038/34097

Scholz, C. H. (2002). The mechanics of earthquakes and faulting (p. 3).

Segall, P. (2010). *Earthquake and volcano deformation* (p. 517). Princeton University Press. https://doi.org/10.1515/9781400833856

Shaw, B. E., Milner, K. R., Field, E. H., Richards-Dinger, K., Gilchrist, J. J., Dieterich, J. H., & Jordan, T. H. (2018). A physics-based earthquake simulator replicates seismic hazard statistics across California. *Science Advances*, *4*(8), 1–10. https://doi.org/10.1126/sciadv.aau0688

Spence, D. A., & Turcotte, D. L. (1979). Viscoelastic relaxation of cyclic displacements on the San Andreas fault. *Proceedings of the Royal Society of London. A. Mathematical and Physical Sciences*, *365*(1720), 121–144.

Suito, H., & Freymueller, J. T. (2009). A viscoelastic and afterslip postseismic deformation model for the 1964 Alaska earthquake. *Journal of Geophysical Research: Solid Earth*, *114*(11), 1–23. https://doi.org/10.1029/2008JB005954

Takeuchi, C. S., & Fialko, Y. (2012). Dynamic models of interseismic deformation and stress transfer from plate motion to continental transform faults. *Journal of Geophysical Research: Solid Earth*, *117*(B5). https://doi.org/10.1029/2011JB009056

Takeuchi, C. S., & Fialko, Y. (2013). On the effects of thermally weakened ductile shear zones on postseismic deformation. *Journal of Geophysical Research: Solid Earth*, *118*(12), 6295–6310. https://doi.org/10.1002/2013JB010215

Tamisiea, M. E., Mitrovica, J. X., & Davis, J. L. (2007). GRACE gravity data constrain ancient ice geometries and continental dynamics over Laurentia. *Science*, *316*(5826), 881–883. https://doi.org/10.1126/science.1137157

Tang, C.-H., Hsu, Y.-J., Barbot, S., Moore, J. D. P., & Chang, W.-L. (2019). Lower-crustal rheology and thermal gradient in the Taiwan orogenic belt illuminated by the 1999 Chi-Chi earthquake. *Science Advances*, *5*(2), eaav3287. https://doi.org/10.1126/sciadv.aav3287

Tarantola, A. (2006). Popper, Bayes and the inverse problem. *Nature Physics*, *2*(8), 492–494. https://doi.org/10.1038/nphys375

Tullis, T. E., Richards-Dinger, K., Barall, M., Dieterich, J. H., Field, E. H., Heien, E. M., et al. (2012). A comparison among observations and earthquake simulator results for the allcal2 California fault model. *Seismological Research Letters*, *83*(6), 994–1006. https://doi.org/10.1785/0220120094

Ulrich, T., Gabriel, A.-A., Ampuero, J.-P., & Xu, W. (2019). Dynamic viability of the 2016 Mw 7.8 Kaikoura earthquake cascade on weak crustal faults. *Nature Communications*, *10*(1), 1–16. https://doi.org/10.31223/OSF.IO/AED4B

Vernant, P. (2015). What can we learn from 20 years of interseismic GPS measurements across strike-slip faults? *Tectonophysics*, *644*, 22–39. https://doi.org/10.1016/j.tecto.2015.01.013

Wang, K., & Fialko, Y. (2018). Observations and modeling of coseismic and postseismic deformation due to the 2015 mw 7.8 Gorkha (Nepal) earthquake. *Journal of Geophysical Research: Solid Earth*, *123*(1), 761–779. https://doi.org/10.1002/2017jb014620

Wen, Y., Li, Z., Xu, C., Ryder, I., & Bürgmann, R. (2012). Postseismic motion after the 2001 mw 7.8 Kokoxili earthquake in Tibet observed by Insar time series. *Journal of Geophysical Research: Solid Earth*, *117*(B8). https://doi.org/10.1029/2011jb009043

Wimpenny, S., Copley, A., & Ingleby, T. (2017). Fault mechanics and post-seismic deformation at bam, se Iran. *Geophysical Journal International*, *209*(2), 1018–1035. https://doi.org/10.1093/gji/ggx065

Yamashita, F., Fukuyama, E., Mizoguchi, K., Takizawa, S., Xu, S., & Kawakata, H. (2015). Scale dependence of rock friction at high work rate. *Nature*, *528*(7581), 254–257. https://doi.org/10.1038/nature16138

Zhao, D., Qu, C., Bürgmann, R., Gong, W., & Shan, X. (2021). Relaxation of Tibetan lower crust and afterslip driven by the 2001 Mw7.8 Kokoxili, China, earthquake constrained by a decade of geodetic measurements. *Journal of Geophysical Research: Solid Earth*, *126*(4), 1–33. https://doi.org/10.1029/2020JB021314

Zheng, G., & Rice, J. R. (1998). Conditions under which velocity-weakening friction allows a self-healing versus a cracklike mode of rupture. *Bulletin of the Seismological Society of America*, *88*(6), 1466–1483.